IDŐJÁRÁS

QUARTERLY JOURNAL
OF THE HUNGARIAN METEOROLOGICAL SERVICE

CONTENTS

****

http://www.met.hu/Journal-Idojaras.php

VOL. 115 * NO. 4 * OCTOBER – DECEMBER 2011

IDŐJÁRÁS

Quarterly Journal of the Hungarian Meteorological Service

Editor-in-Chief
LÁSZLÓ BOZÓ

Executive Editor
MÁRTA T. PUSKÁS

EDITORIAL BOARD

AMBRÓZY, P. (Budapest, Hungary)
ANTAL, E. (Budapest, Hungary)
BARTHOLY, J. (Budapest, Hungary)
BATCHVAROVA, E. (Sofia, Bulgaria)
BRIMBLECOMBE, P. (Norwich, U.K.)
CZELNAI, R. (Dörgicse, Hungary)
DUNKEL, Z. (Budapest, Hungary)
FISHER, B. (Reading, U.K.)
GELEYN, J.-Fr. (Toulouse, France)
GERESDI, I. (Pécs, Hungary)
GÖTZ, G. (Budapest, Hungary)
HASZPRA, L. (Budapest, Hungary)
HORÁNYI, A. (Budapest, Hungary)
HORVÁTH, Á. (Siófok, Hungary)
HORVÁTH, L. (Budapest, Hungary)
HUNKÁR, M. (Keszthely, Hungary)
LASZLO, I. (Camp Springs, MD, U.S.A.)
MAJOR, G. (Budapest, Hungary)
MATYASOVSZKY, I. (Budapest, Hungary)
MÉSZÁROS, E. (Veszprém, Hungary)
MIKA, J. (Budapest, Hungary)
MERSICH, I. (Budapest, Hungary)
MÖLLER, D. (Berlin, Germany)
NEUWIRTH, F. (Vienna, Austria)
PINTO, J. (Res. Triangle Park, NC, U.S.A.)
PRÁGER, T. (Budapest, Hungary)
PROBÁLD, F. (Budapest, Hungary)
RADNÓTI, G. (Reading,U.K.)
S. BURÁNSZKI, M. (Budapest, Hungary)
SIVERTSEN, T.H. (Risør, Norway)
SZALAI, S. (Budapest, Hungary)
SZEIDL, L. (Budapest, Hungary)
SZUNYOGH, I. (College Station, TX, U.S.A.)
TAR, K. (Debrecen, Hungary)
TÄNCZER, T. (Budapest, Hungary)
TOTH, Z. (Camp Springs, MD, U.S.A.)
VALI, G. (Laramie, WY, U.S.A.)
VARGA-HASZONITS, Z. (Moson-magyaróvár, Hungary)
WEIDINGER, T. (Budapest, Hungary)

Editorial Office: Kitaibel P.u. 1, H-1024 Budapest, Hungary
P.O. Box 38, H-1525 Budapest, Hungary
E-mail: journal.idojaras@met.hu
Fax: (36-1) 346-4669

Indexed and abstracted in Science Citation Index Expanded™ and Journal Citation Reports/Science Edition
Covered in the abstract and citation database SCOPUS®

Subscription by

mail: IDŐJÁRÁS, P.O. Box 38, H-1525 Budapest, Hungary
E-mail: journal.idojaras@met.hu

IDŐJÁRÁS

Quarterly Journal of the Hungarian Meteorological Service
Vol. 115, No. 4, October–December 2011, pp. 219–232

Weather induced variability of nitrogen exchange between the atmosphere and a grassland in the Hungarian Great Plain

Attila Machon[*1,2,4], **László Horváth**[1], **Tamás Weidinger**[3], **Krisztina Pintér**[4,5], **Balázs Grosz**[3], **Zoltán Nagy**[4,5], and **Ernő Führer**[6]

[1]*Hungarian Meteorological Service, Gilice tér 39, H-1181 Budapest, Hungary*

[2]*Center for Environmental Science, Eötvös Loránd University, Pázmány P. sétány 1/A, H-1117 Budapest, Hungary*

[3]*Departement of Meteorology, Eötvös Loránd University, Pázmány P. sétány 1/A, H-1117 Budapest, Hungary*

[4]*Institute of Botany and Ecophysiology, Szent István University, Páter Károly utca 1, H-2103 Gödöllő, Hungary*

[5]*Plant Ecology Research Group of Hungarian Academy of Sciences, Páter Károly utca 1, H-2103, Gödöllő, Hungary*

[6]*Hungarian Forest Research Institute, Paprét 17, H-9400 Sopron, Hungary*

[*]*Corresponding author; E-mail: machon@caesar.elte.hu*

(Manuscript received in final form October 21, 2011)

Abstract—The paper describes some of the preliminary results of the ecological research on nitrogen exchange in a grassland in central Hungary (Kiskunság National Park, Bugacpuszta). The changes in different climate parameters evidently affect not only N-deposition but also N-exchange and N-gas emissions through the processes of soil and plant metabolism. Measurements of nitrogen fluxes and basic meteorological parameters have been started above a semi-natural grassland ecosystem in 2002. Seasonal and long-term nitrogen exchange (both emission and deposition) is under climatic control. In the years of 2006 and 2007, the amount of the deposited N markedly decreased (by 27% and 15%, respectively) compared to the average of the earlier (2002–2004) years. The main source of the deposited N is NH_3. The ratio of dry to wet deposition varies between 1.5 and 2.3. In the dry year of 2007, emissions of N_2O were four times lower compared to the

average (90 mg N m^{-2} yr^{-1}) of the earlier years caused by the changes in weather conditions including lower precipitation and 1 °C higher annual average temperature. In the year with higher precipitation (2010), N_2O emissions increased again and reached 180 mg N m^{-2} yr^{-1} when the annual rainfall was twice the normal rate. It should be noted that soil water filled pore space (WFPS) cannot explain all of the variations in N_2O fluxes. With increasing soil temperature, NO flux grows faster than N_2O up to 20 °C until the role of other factors (e.g., water stress, nutrient supply, and other complex processes linked to heat stress) will determine the magnitude of metabolism. The relatively high soil N_2O flux under 5 °C could come from the thawing period 2–3 months after wintertime which could resulting in high emission peaks for a few days with low soil temperature. It seems to be the case that soil temperature usually generates short term variability of trace gas exchange, whereas the magnitude of the biogenic emission is dominantly controlled by soil wetness, pH, and other site specific factors. The net N flux – excluding grazing, manure, farm management, etc. – ranged between 9.5 and 13 kg N ha^{-1} yr^{-1}. Reduced N_2O emission presents a potential negative feedback to emission; on the other hand, vegetation can become a net CO_2 source in extremely dry years such as 2003 and 2007 as a positive feedback to climate change.

Key-words: N-exchange, N-emission, N-deposition, climate perturbation, grassland, denitrification

1. Introduction

The climate in middle and southern Europe will likely be warmer, with drier summers; in some parts with shorter or mild and wetter winters, and more variable patterns of rainfall and temperature in the 21st century as predicted by *EEA* (2004). Grasslands are one of the most widespread vegetation types in Europe and, especially, in the Hungarian Great Plain, which also appear to be drifting to desertification. This is an important environmental problem, because grassland ecosystems are important in the cycle of nitrogen (N) and carbon (C) between the land surface and the atmosphere. Sensitivity of N balance of grasslands to climatic perturbations such as drought remains uncertain (*Schimel et al.*, 1996; *Reich et al.*, 2006).

Interactions between climate perturbations and changing dynamics of N-cycle of grasslands have received much less attention than the C-cycle and corresponding interactions in forests. Some studies were carried out for Hungarian grassland sites on how net ecosystem exchange (NEE) of carbon dioxide, respiration processes (*Balogh et al.*, 2005, 2008), or the greenhouse gas (GHG) flux will change as a consequence of climate change (*Nagy et al.*, 2005, 2007). The markers such as heat and drought extremes – which will become on more frequent as a result of the climate perturbations – can also have an impact the nitrogen budget through trace gas soil fluxes as well as the carbon and water balance (*Pintér et al.*, 2008) due to soil functioning, and they may lead to reduced plant growth or changes in grassland species composition. Some European studies pointed out the effects of soil condition on NO, NO_2, and N_2O emission from different soils (*Schindlbacher et al.*, 2004) or on CH_4 uptake by sandy grassland

ecosystems (*van den Pol-van Dasselaar et al.*, 1998). Many aspects of the relation between N and C cycles (e.g., *Soussana* and *Hartwig*, 1996), estimation of the nitrogen and carbon fluxes (*Levy et al.*, 2007) and budgets (*Ammann et al.*, 2009; *Skiba et al.*, 2009) in grassland were also studied.

The changed weather condition – through the changes of soil conditions (e.g., soil temperature, humidity etc.) – greatly affects the soil processes like mineralization, decomposition, nitrification, and denitrification as the significant sources and controllers of atmospheric C and N trace gases (*Conrad*, 1996) and the sink of NH_4^+ and NO_3^- substrates. Due to the processes above, the organic/inorganic N pool of soil or soil emission of NO, N_2O, as well as N uptake of plants are subject to change. These processes are linked with other stressors (e.g., heat stress, water deficiency, etc.) and may easily influence plant physiology, productivity or plant species composition.

The objective of this work is to investigate the nitrogen exchange between atmosphere and grassland and its dependence on climatic conditions, and focusing on links with reactive trace gas emissions and N-deposition, and on the possible feedbacks to soil-vegetation dynamics.

2. Materials and methods

Investigations were conducted at the *Bugacpuszta* nature reserve research site (46.69 °N, 19.60 °E, h = 110 m asl) in the Hungarian Great Plain. Measurements of nitrogen fluxes and basic micrometeorological parameters above a semi-natural ecosystem were started in 2002. This station also provides input data for modeling, validation, and calibration of models. The climate is continental with annual average temperature of 10.5 °C, and the average precipitation is about 530 mm year^{-1}. The vegetation is semi-arid sandy grassland *(Cynodonti Festucetum pseudovinae)* where *Festuca pseudovina, Carex stenophylla, Salvia pratensis*, and *Cynodon dactylon* are the dominant plant species. The landscape is flat. The soil is a Chernozem-type sandy soil (*Machon et al.*, 2010) (sand : silt : clay = 82 : 7 : 11% is the average composition of the top 20 cm soil).

Soil emission of NO has been determined by dynamic chamber method as described in *Horváth et al.* (2006). Soil N_2O flux measurements were carried out bi-weekly (2002–2004), later weekly (2006–2010) by 8 parallel static soil chambers (*Clayton et al.*, 1994; *Christensen et al.*, 1996). Samples were taken at t = 0, 15, and 30 minutes after closure of chambers. Concentration changes (within 30 min) were determined by gas chromatography-mass spectrometry (GC-MS). According to statistical analysis, the non-systematic bulk error (CV: coefficient of variation) of sampling and analysis, estimated using parallel sampling, was always below 10%. In 2007, the detector was changed to electron capture (GC-ECD). Three-stage filter pack method was used for daily sampling of particles and gases followed by ion-chromatograpy (nitrate, nitric acid) and

spectrophotometry (indophenol-blue method for ammonium and ammonia) (*EMEP*, 1996). The minimum detection limit (MDL) is 0.1 $\mu g\,N\,m^{-3}$ for all components. The precision (bulk relative error) of sampling and measurements was around 10%. Dry deposition of nitrogen dioxide, ammonia, nitric acid vapour, nitrate, and ammonium particles were inferred using dry deposition velocities (*Horváth et al.*, 2005) measured above surfaces with the same characteristics as those of Bugacpuszta station. Fluxes of NH_3, within the atmosphere and the canopy (excluding soil emission) were also inferred this way. Wet depositions of nitrate and ammonium ions were calculated on the basis of daily precipitation sampling and concentration measurements of amonium and nitrate ions by the analytical mehtods described in *Machon et al.* (2010). The calculated bulk error of precipitation sampling and concentration measurements was around 10%. Minimum detection limit was 0.05 $mg\,N\,L^{-1}$ for both ions. Meteorological parameters like precipitation, air and soil temperature, and soil moisture were also observed.

3. Results and discussion

The studied sandy grassland soil has poor water supply with deep water table (6 m). In summer months, high ground surface temperatures can be observed (>30 °C) and the upper layer of soil dries out. Nitrate leaching is estimated to be negligible. Suction cups applied below rooting zone did not collect measurable quantity of soil water. The soil N trace gas production depends strongly on soil biology, chemistry, and physics (*Smith et al.*, 2003). Denitrification is stimulated by hypoxia. In dry soils (down to water filled pore space (WFPS) of about 30%, see *Fig. 1*) this process is limited due to the unfavorable soil conditions for the anaerobic microbial communities (nitrous oxide production and subsequent emission rate are maximized at WFPS range of 40–50% (*Horváth et al.*, 2010)). In drier soils, in the well aerated zone, the nitrification is the dominant process producing NO.

During the summer, microbial productivity is elevated (mineralization, nitrification, immobilization, decomposition, etc.), but denitrification (N_2O production) is suppressed when the WFPS is low. In dormant period, despite the higher WFPS, the activity of microbial community decreases in parallel with soil temperature decrease, resulting in low N_2O production.

Changes in seasonality, distribution, and frequency of precipitation and the total amount of rainfall may have an impact greatly on the nitrogen exchange of this ecosystem, resulting in a switch between the N_2O and NO production (determined by soil processes). Both seasonal and long-term nitrogen exchanges of this ecosystem is, therefore, linked to the soil water content (due to rainfall regime) and soil temperature (*Machon et al.*, 2010). *Fig. 1* shows that higher soil NO emissions were observed in comparison to N_2O in the dry soil in summer

seasons, especially in 2007. During summers, the WFPS ranged between 20–30% (with exception of 2010). In 2007, the average soil wetness was 19%, close to the optimum for NO production by nitrification processes. Nitrification processes were dominating this year and NO emission (70 mg N m^{-2} yr^{-1}) was higher than N_2O soil flux (15 mg N m^{-2} yr^{-1}); later it significantly decreased compared to the earlier (2002–2004) years when average emission was 90 mg N m^{-2} yr^{-1} (*Flechard et al.,* 2007). In recent years, similar significantly lower emissions of N_2O were observed at different types of grasslands in Hungary (*Horváth et al.,* 2008), in comparison to 2002–2004, on the basis of weekly sampling. In 2010, N_2O emissions (180 mg N m^{-2} yr^{-1}) exceeded NO emissions (78 mg N m^{-2} yr^{-1}) due to the unusually high precipitation and WFPS in summer months, favoring denitrification metabolisms.

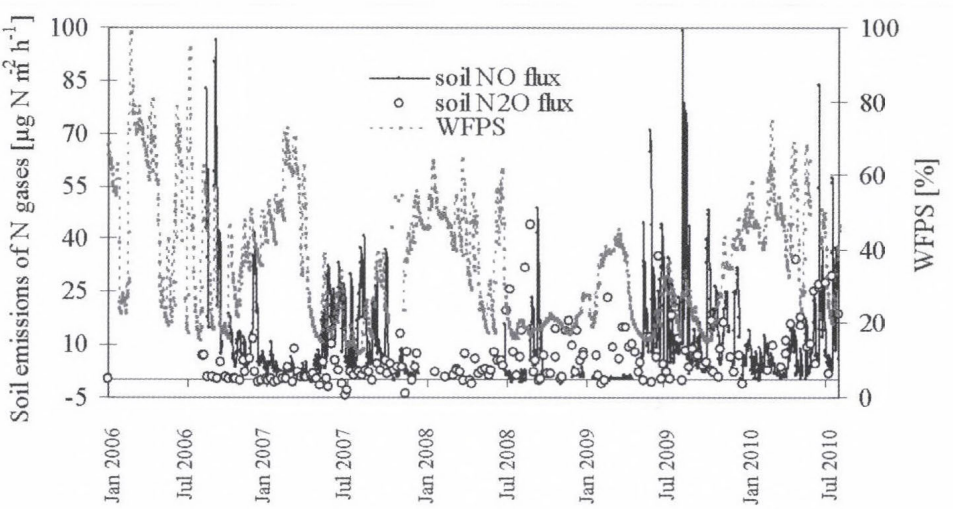

Fig. 1. Soil N gases emissions and linkage to soil humidity (WFPS) at Bugacpuszta station. (Due to instrument failure, there are only a few data points for soil NO flux in 2008.)

Trace gas emissions and N-deposition can be highly variable from season-to-season or year-to-year, but available parameters such as air and soil temperature, precipitation, and soil moisture more or less can explain this variability. Some uncertainty may arise from the complexity of soil and atmospheric processes and/or accuracy of measurements.

It can clearly be seen in *Table 1*, that emission of N_2O decreases by a factor of 4 in 2006 and 2007 and increases by a factor of two in 2010 compared to the earlier (2002–2004) measurements at the same place. This phenomenon is explainable by soil microbial processes, as the rate of denitrification, etc., strongly depends on the varying weather conditions (e.g., water or heat stress). In 2009, the annual mean temperature was the same as in 2008, but this year was

drier. In contrast, substantial decrease was not observed in the measured flux. It can be explained partly by the fact that the sandy soil dried out within a short time after the rain events, and the effective time for denitrifying bacteria, preferring anaerobic condition, was shorter than in wet soils with higher water retaining capacity. On the other hand, in extremely wet soils emission of nitrous oxide is limited, and reduction leads to production of di-nitrogen (N_2). The weather conditions (e.g., abiotic stress) prevent optimum soil condition for nitrous oxide production to be sustained for long periods during the study.

Table 1. Annual sum of climatic conditions and N-exchange [mg N m^{-2} yr^{-1}] between the surface and atmosphere at Bugacpuszta station

Measured parameters	**2002–2004**	**2006**	**2007**	**2008**	**2009**	**2010**
Precipitation [mm]	545	524	446	567	486	967
WFPS mean [%]		34.6	33.6	30.2	27.9	43
(SD)		± 11.7	± 16.6	± 13.9	± 9.67	± 12
T_{air}, mean [°C]	10.1	10.1	11.1	11.0	11.2	11
$T_{soil\ (5cm)}$, mean [°C]		10.2	11.5	11.1	11.4	10.9
(SD)		± 6.6	± 4.5	± 3.7	± 3.7	
Wet (NO_3^- and NH_4^+) deposition	–470	–338	–420	–520	–450	–578
(SD)	± 23[a]	± 17	± 21	± 26	± 23	± 29
Dry HNO_3 deposition	–320	–157	–172	–264	–235	–295
(SD)	± 32[a]	± 16	± 17	± 26	± 24	±30
Dry NH_3 deposition	–460	–418	–454	–532	–425	–379
(SD)	± 23[a]	± 21	± 23	± 27	± 21	± 19
Dry NO_3^- and NH_4^+ deposition	–130	–136	–85	–109	–116	–104
(SD)	± 7[a]	± 7	± 4	± 5	± 6	± 5
Dry NO_2 deposition	–75[b]	–75	–45	–80	–79	–95
(SD)		± 4	± 2	± 4	± 4	± 5
Soil N_2O emission	80[c]	18	15	56	63	180
Soil NO emission	119[d]	160	79	119[d]	118	78
Total deposition	–1.455	–1.124	–1.176	–1.505	–1.305	–1.451
Sum of net N flux	**–1.256**	**–946**	**–1.082**	**–1.330**	**–1.124**	**–1.193**

[a] *Kugler et al.*, 2008

[b] Estimated from the average of 2006–2010

[c] *Horváth et al.*, 2010

[d] No data for technical reason, calculated from the mean NO emission for 2006–2007 and 2009

Wet deposition of nitrate and ammonium together with the dry flux of ammonia and nitric acid vapor are responsible for the majority (80%) of the net N budget.

The sum of the atmospheric N-deposition (excluding deposited organic N) varied between 1.1 and 1.5 mg N m^{-2} yr^{-1}. It is noteworthy, that the precipitation amount nearly doubled in 2010 (see in *Table 1*), nevertheless, the wet deposition does not follow this pattern. Ratio of dry to wet deposition varied in the range of 1.5–2.3. According to the results (*Fig. 2*), in 2007 and 2009 the annual precipitation amount was significantly lower, and in 2010 it was two times higher than the long term mean. The deficit in the yearly precipitation mainly occurred in July in the vegetation period of 2006–2009 (see *Fig. 3*) resulting in less biomass production, because the drought and the main growing period coincided. At the same time, the lack of precipitation affects the N-cycle through missing wet deposited N, plant uptake, water stress, and other soil processes. In 2007, the annual mean temperature has increased by 1 °C associated with mild winter (soil frost occurred rarely) and less number of rain events were observed. In 2008, the amount of precipitation reached the regular level, but the annual mean temperature remained 1 °C higher as in 2007. The year of 2010 had extra amount of precipitation (it was one of the most wet of the last 100 years; http://www.met.hu) and differs from the long-term statistical averages (see in *Figs. 2* and *3*). For this reason, all the circumstances and conditions are different from the previous years.

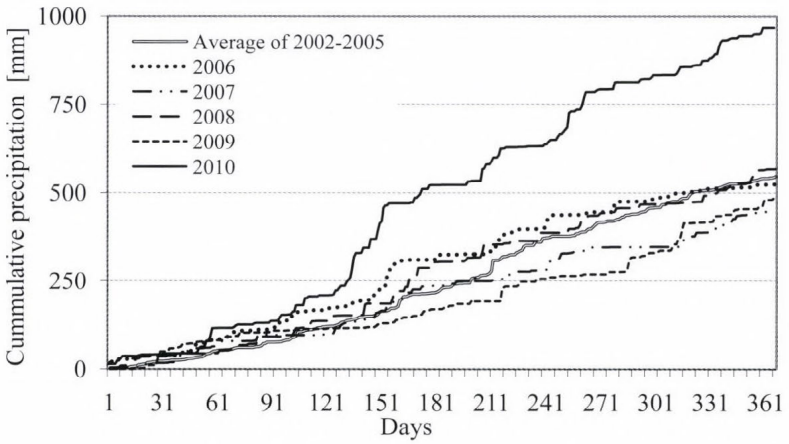

Fig. 2. Cumulative precipitation for the last decade at Bugacpuszta station.

N-compounds can easily be leached into the soil by rain, while canopy can retain dry deposited nitrogen through the N-uptake by stomatae or cuticles, which also depends on the meteorological conditions (*Horváth et al.*, 1999). For this reason, in drier years less amount of deposited, reaches the topsoil layers

nitrogen and it can limit the mineral N-conversion to gases (through denitrification and nitrification processes). Reduced availability of soil mineral nitrogen may limit the plant uptake and probably impacts on the plant physiology and biomass production of different species; nevertheless, changes of plant species composition or coverage of plant functional group are not observed. Further research of N-linkage to the coenological experiment of grassland association is needed in the future.

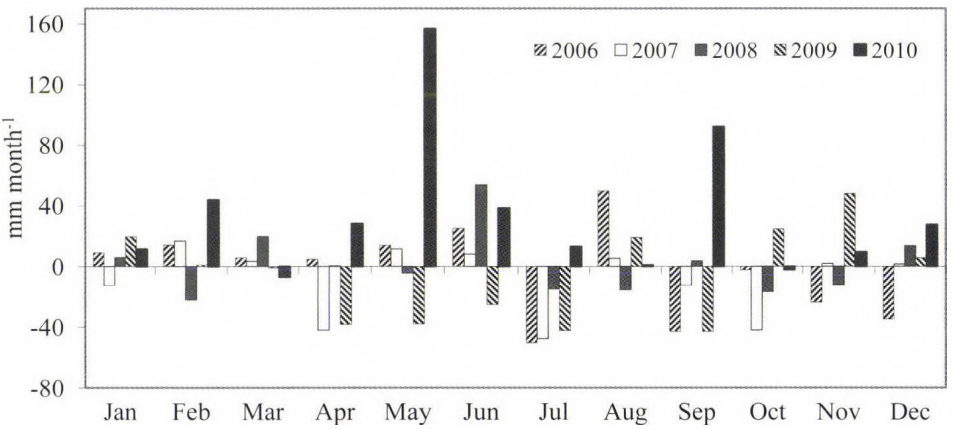

Fig. 3. Deviation of monthly precipitation of the studied years from the average of long term period (1986–2006) at Bugacpuszta station.

NO and N_2O soil emissions as consequences of nitrification and denitrification are, like all biological processes, influenced by temperature and correlate with the soil temperature as many studies discussed before (*Smith et al.*, 1998; *Gödde* and *Conrad*, 1999; *Horváth et al.*, 2010), but sometimes the correlation remains poor or not readily understandable (*Clayton et al.*, 1997). With increasing soil temperature, the NO flux increases faster than N_2O up to 20 °C; until the role of other factors (e.g., water stress, nutrient supply, and other complex processes linked to heat stress) will determine the rate of metabolism of soil microorganisms (see *Fig. 4*). The relatively high soil N_2O flux under 5 °C could be the reason of thawing period after 2-3 month wintertime which resulting in high emission peaks for a few days even at low soil temperature (*Priemé* and *Christensen*, 2001; *Müller et al.*, 2002).

The optimal soil wetness for NO and N_2O is ranged around 20–30% and 40–50%, respectively (see *Fig. 5*) for this sandy soil. The optimal WFPS content is reached only in 2010 for N_2O. High water content (WFPS>70%) was rarely observed, so the dependence of N-gas production on soil humidity is incomplete, but we expect (according to earlier studies) that emissions of both gases are continuously suppressed with higher WFPS content (*Horváth et al.*, 2010).

It should be noted that the soil water filled pore space can not explain all of the variations of N_2O fluxes (see *Fig. 4b*). It seems to be more likely, that soil temperature usually generate short-term variations of the trace gas exchange, whereas the magnitude of the biogenic emission is predominantly influenced by soil wetness, and other factors (*Meixner* and *Yang*, 2004).

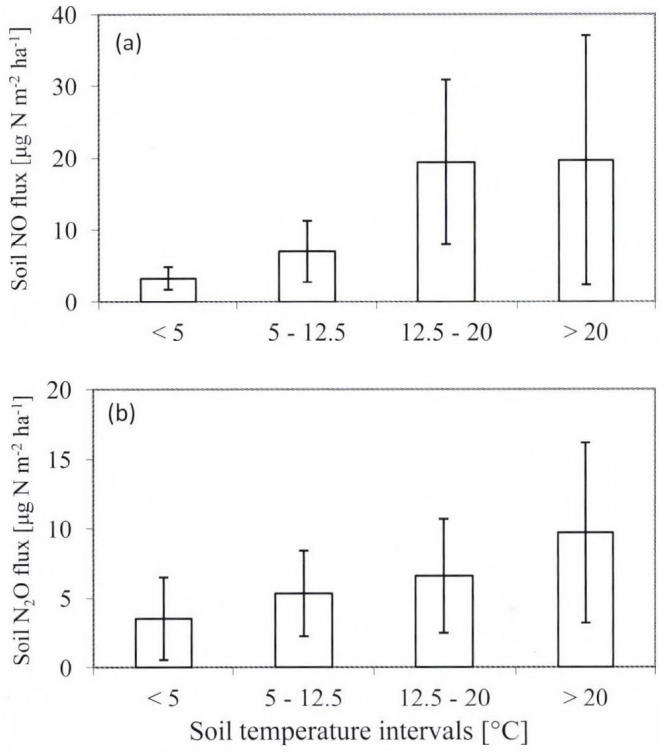

Fig. 4. Variation of nitric oxide flux (a) and nitrous oxide flux (b) as a function of soil temperature at Bugacpuszta station.

On the other hand, *Kool et al.* (2007, 2009a) studied our soils by incubation technique using isotope tracers of oxygen and nitrogen, when O-exchange between water and intermediate forms of the N-transformations were measured. By this novel approach they showed that nitrifier denitrification (nitrite reduction by ammonia oxidizers) can be a contributor to the majority of N_2O production at Bugacpuszta site, thus, N_2O can be produced at lower water content – this phenomenon may explain the secondary higher emission on low (20–30%) WFPS – see in *Fig. 5b*. This biochemical pathway also demonstrates that pH may be the major factor determining nitrifier-induced N_2O production,

and the community of microorganisms may not be the key driver in different pathways of N_2O formation (*Kool et al.*, 2010). By this methodology it was also observed that water is effectively the main oxygen source (instead of O_2 as it was assumed earlier) in N_2O formation and possibly in the formation of other nitrogen oxides in some European soil samples including Bugacpuszta. The oxygen isotopic measurement of N_2O showed that in Bugacpuszta the soil NH_4^+ can be the nitrogen source (and it does not necessarily reflect that NO_3^- is functioning as a substrate) in N_2O formation though the nitrifier denitrification as an alternative pathway of metabolism of microorganisms (*Kool et al.*, 2009b). Further investigations are needed for better understanding the metabolism processes.

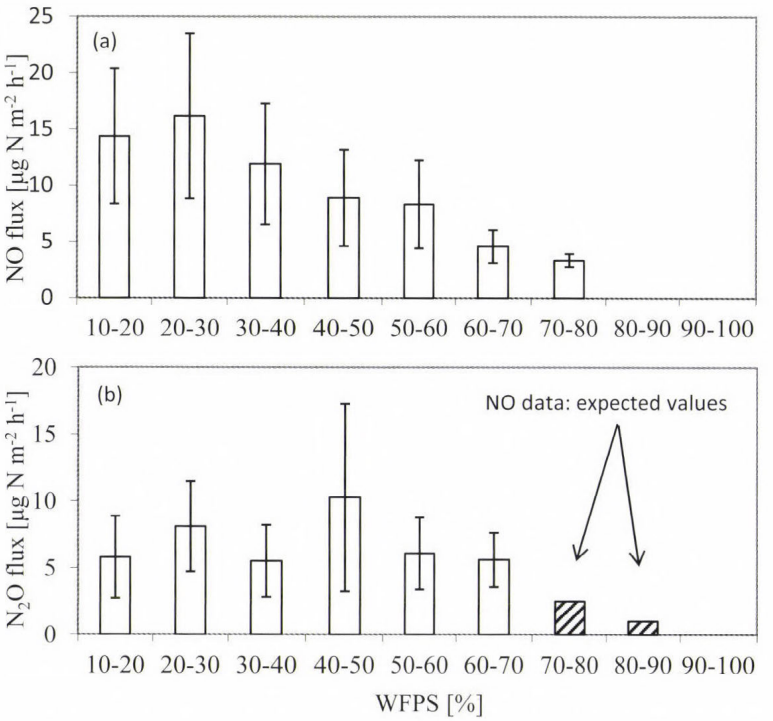

Fig. 5. Variation of nitric oxide flux (a) and nitrous oxide flux (b) as a function of water filled pore space at Bugacpuszta station.

The changes in N-exchange may impact on the carbon cycle as well as on plant uptake leading to opening up and desertification of the grassland, in spite of the fact that the studied ecosystem is evolved and more adapted to drought (in terms of NEE, etc.) than other grasslands (*Pintér et al.*, 2008).

4. Conclusions

Weather perturbations can substantially modify both timing and magnitude of N-deposition and soil N-gas emission. In summertime, parallel with the precipitation deficit, less easily available nitrogen is deposited to the surface leaching to the rooting zone; thus, it can limit the mineral N uptake by plants or may affect the soil emission (through suppress of microbial processes) of N-gases during the main vegetation period.

Summarizing, many soil process (e.g., nitrification, denitrification, N-leaching) are strongly depend on soil temperature and precipitation as ecological drivers. The changes in these parameters influence directly the soil nitrogen gas emission rates, though the complex system of the relationships makes it difficult to explain all changes of NO and N_2O formation. Though NO flux was higher than N_2O flux, the soil emission was an order of magnitude lower than the atmospheric deposition (see *Table 1*).

The seasonal fluctuation of N_2O and NO emission has been mainly influenced by precipitation. N_2O emissions were not significant in the N-budget at this site in the last years. Reduced N_2O emission (occurring through desertification due to perturbed climate conditions) means a potential negative feedback to the greenhouse effect. On the other hand, the vegetation can turn into being a net CO_2 source in extremely dry years like 2003 and 2007 (*Pintér et al.*, 2008; *Barcza et al.*, 2009) as a positive feedback for climate change. The ratio and strength of this two phenomena can not be neglected, since the area of temperate grass covered surface is large and will be increasing with increasing aridity of climate (and/or agricultural policy of Hungary). Extended periods of soil water deficit and high air and soil temperatures can affect a wide range of plant physiological functions. The plant communities will be frequently exposed to naturally induced droughts and should become open grassland in accordance with the value of the changing weather conditions.

Due to the forecasted potentially drying Hungarian climate, more frequent natural fires, as ecosystem function distractions, will occur in the dry sandy grassland (Hungarian Great Plain). The estimated nitrogen loss by fires equals to or even exceeds the amount of nitrogen from atmospheric deposition.

Based on the observed phenomena, it can be concluded that climate extremes are significant factors in soil organism functioning and dynamics of N-exchange and emissions. As a result, the N-content of the soil is continuously changing with the climatic anomalies (*Czóbel et al.*, 2008) due to the pool of NH_4^+ and NO_3^- – which depends on the N-consumption and exchange of soil microbial community – affecting the plant N-uptake (demand), plant growth, etc. The living roots and bacteria are competitors for the same nutrients, so plants also induce effect on soil N-transformations. Further research relating to soil biochemistry in natural grasslands is also needed. Compared to the average of earlier years (13.8 kg N ha^{-1}; *Kugler et al.*, 2008), less nitrogen deposited onto

the surface (11.2 and 11.7 kg N ha^{-1}) in the driest period (2006 and 2007) and more nitrogen deposited (15.0 and 14.5 kg N ha^{-1}) in the wetter years (2008 and 2010) during the study period. Wet deposition of nitrate and ammonium together with the dry flux of ammonia and nitric acid vapor is responsible for the majority (80%) of the net N-deposition flux. Seasonal and annual variation of N-gas emissions and N-deposition can be considerable, but precipitation, soil moisture, air and soil temperature, as easily measured parameters, can more or less explain this variability.

Acknowledgements—The authors are grateful for the permission of the Management of Kiskunság National Park to conduct the studies in the territory of the national park near Bugacpuszta. This work has been supported by the NitroEurope Framework EU 6th IP, by the National Research and Innovation Programs (NKFP/088/2004, NKFP6- 00028/2005 and NKFP6-00079/2005), COST Action 0804, and partly supported by the European Union and co-financed by the European Social Fund grant agreement (No. TAMOP 4.2.1/B-09/1/KMR-2010-0003).

References

Ammann, C., Spirig, C., Leifeld, J., and *Neftel, A.*, 2009: Assessment of the nitrogen and carbon budget of two managed temperate grassland fields. *Agr. Ecosyst. Environ. 133,* 150–162.

Balogh, J., Czóbel, Sz., Fóti, Sz., Nagy, Z., Szirmai, O., Péli, E. and *Tuba, Z.*, 2005: The influence of drought on carbon balance in loess grassland. *Cereal Res. Commun. 33,* 149–152.

Balogh, J., Biró, M. and *Pintér, K.*, 2008: Root respiration in dry grassland. *Cereal Res. Commun. 36,* Supl. 355–358.

Barcza, Z., Haszpra, L., Somogyi, Z., Hidy, D., Lovas, K., Churkina, G. and *Horváth, L.*, 2009: Estimation of the biospheric carbon dioxide balance of Hungary using the BIOME-BGC model. *Időjárás 113*, 203–219.

Clayton, H., Arah, J.R.M. and *Smith, K.A.*, 1994: Measurement of nitrous oxide emissions from fertilized grassland using closed chambers. *J. Geophys. Res. 99*, 16599–16607.

Clayton, H., McTaggart, I.P., Parker, J., Swan, L. and *Smith, K.A.*, 1997: Nitrous oxide emission from fertilized grassland: A 2-year study of the effects of N fertilizer form and environmental conditions. *Biol. Fertil. Soils 25*, 252–260.

Christensen, S., Ambus, P., Arah, J.R.M., Clayton, H., Galle, B., Griffith, D.W.T., Hargreaves, K.J., Klemedtsson, L., Lind, A.-M., Maag, M., Scot, A., Skiba, U., Smith, K.A., Welling, M. and *Wienhold, F.G.*, 1996: Nitrous oxide emission from an agricultural field: comparison between measurements by flux chamber and micro-meteorological techniques. *Atmos. Environ. 30*, 4183–4190.

Conrad, R., 1996: Soil Microorganisms as controllers of atmospheric trace gases (H_2, CO, CH_4, OCS, N_2O, and NO). *Microbiological Reviews 60*, 609–640.

Czóbel, Sz., Balogh, J., Fóti, Sz. and *Szirmai, O.*, 2008: Temporal changes in biomass and soil element contents under different manipulations of temperate grassland. *Cereal Res. Commun. 36,* 1963–1966.

EEA (European Environment Agency), 2004: *Impacts of Europe's changing climate. An indicator-based assessment.* Luxembourg, Office for Official Publications of the European Communities — pp. 107, ISBN 92-9167-692-6.

EMEP, 1996: Manual for sampling and chemical analysis. EMEP/CCC-Report 1/95, NILU, Kjeller, Norway.

Flechard, C.R., Ambus, P., Skiba, U., Rees, R.M., Hensen, A., van Amstel, A., van den Pol-van Dasselaar, A., Soussana, J.-F., Jones, M., Clifton-Brown, J., Raschi, A., Horvath, L., Neftel, A., Jocher, M., Ammann, C., Leidfield, J., Fuhrer, J., Calanca, P.L., Thalman, E., Pilegaard, K., Di Marco, C., Campbell, C., Nemitz, E., Hargreaves, K.J., Levy, P., Ball, B.C., Jones, S., van de Bulk, W.C.M.,

Groot, T., Blom, M., Domingues, R., Kasper, G., Allard, V., Ceshia, E., Cellier, P., Laville, P., Henault, C., Bizouard, F., Abdalla, M., Williams, M., Baronti, S., Berretti, F. and *Grosz, B.*, 2007: Effects of climate and management intensity on nitrous oxide emissions in grassland systems across Europe. *Agr. Ecosyst. Environ. 121*, 135–152.

Gödde, M. and *Conrad, R.*, 1999: Immediate and adaptational temperature effects on nitric oxide production and nitrous oxide release from nitrification and denitrification in two soils. *Biol. Fertil. Soils 30*, 33–40.

Horváth, L., Christensen, S., Führer, E., Kelecsényi, S., Mészáros, R., Nagy, Z. and *Weidinger, T.*, 1999: A preliminary estimation of the nitrogen compounds exchange between the atmosphere and a Spruce forest. *Időjárás 103*, 1–18.

Horváth, L., Asztalos, M., Führer, E., Mészáros, R. and *Weidinger, T.*, 2005: Measurement of ammonia exchange over grassland in the Hungarian Great Plain. *Agr. Forest Meteorol. 130*, 282–298.

Horváth, L., Führer, E. and *Lajtha, K.*, 2006: Nitric oxide and nitrous oxide emission from Hungarian forest soils; linked with atmospheric N-deposition. *Atmos. Environ. 40*, 7786–7795.

Horváth, L., Grosz, B., Machon, A., Balogh, J., Pintér, K. and *Czóbel, Sz.*, 2008: Influence of soil type on N_2O and CH_4 soil fluxes in Hungarian grasslands. *Community Ecol. 9* (Suppl): 75–80.

Horváth, L., Grosz, B., Machon, A., Tuba, Z., Nagy, Z., Czóbel, Sz., Balogh, J., Péli, E., Fóti, Sz., Weidinger, T., Pintér, K. and *Führer, E.*, 2010: Estimation of nitrous oxide emission from Hungarian semi-arid sandy and loess grasslands; effect of grazing, irrigation and application of fertilizer. *Agr. Ecosyst. Environ. 139*, 255–263.

Kool, D.M., Wrage, N., Oenema, O., Dolfing, J. and Van *Groenigen, J.W.*, 2007: Oxygen exchange between (de)nitrification intermediates and H_2O and its implications for source determination of NO_3^- and N_2O: a review. *Rapid Commun. Mass Spectrom. 21*, 3569–3578.

Kool, D.M., Müller, C., Wrage, N., Oenema, O. and *Van Groenigen, J.W.*, 2009a: Oxygen exchange between nitrogen oxides and H_2O can occur during nitrifier pathways. *Soil Biol. Biochem. 41*, 1632–1641.

Kool, D.M., Wrage, N., Oenema, O., Harris, D. and *Van Groenigen, J.W.*, 2009b: The 18O signature of biogenic nitrous oxide is determined by O exchange with water. *Rapid Commun. Mass Spectrom. 23*, 104–108.

Kool, D.M., Wrage, N., Zechmeister-Boltenstern, S., Pfeffer, M., Brus, D., Oenema, O., Van Groenigen, J.W., 2010: Nitrifier denitrification can be a source of N_2O from soil: a revised approach to the dual isotope labelling method. NitroEurope Open Science Conference: Reactive Nitrogen and the European Greenhouse Gas Balance. February 3–4, 2010, Solothurn, Switzerland. Book of abstracts: pp. 12.

Kugler, Sz., Horváth, L. and *Machon, A.*, 2008: Estimation of nitrogen balance between the atmosphere and Lake Balaton and a semi natural grassland in Hungary. *Environ. Pollut. 154*, 498–503.

Levy, P.E., Mobbs, D.C., Jones, S.K., Milne, R., Campbell, C. and *Sutton, M.A.*, 2007: Simulation of fluxes of greenhouse gases from European grasslands using the DNDC model. *Agr. Ecosyst. Environ. 121*, 186–192.

Machon, A. Horváth, L., Weidinger, T., Grosz, B., Pintér, K., Tuba, Z. and *Führer, E.*, 2010: Estimation of net nitrogen flux between the atmosphere and a semi-natural grassland ecosystem in Hungary. *Eur. J. Soil Sci. 61*, 631–639.

Meixner, F.X. and *Yang, W.X.*, 2004: Biogenic emissions of nitric oxide and nitrous oxide from arid and semi-arid land. In *Dryland Ecohydrology*, (eds.: *P. D'Odorico* and *A. Porporato,*), pp. 23–46. Kluwer Academic Publishers B.V., Dordrecht, Netherlands.

Müller, C., Martin, M., Stevens, R.J., Laughlin, R.J., Kamman, C., Ottow, J.C.G. and *Jager, H.J.*, 2002: Processes leading to N_2O emissions in grassland soil during freezing and thawing. *Soil Biol. Biochem. 34*, 1325–1331.

Nagy, Z., Czóbel, Sz., Balogh, J., Horváth, L., Fóti, Sz., Pintér, K., Weidinger, T., Csintalan, Zs. and *Tuba Z.*, 2005: Some preliminary results of the Hungarian grassland ecological research: carbon cycling and greenhouse gas balances under changing. *Cereal Res. Commun. 33*, 279–281.

Nagy, Z., Pintér, K., Czóbel, Sz., Balogh, J., Horváth, L., Fóti, Sz., Barcza, Z., Weidinger, T., Csintalan, Zs., Dinh, N.Q., Grosz, B. and *Tuba, Z.*, 2007: The carbon budget of semi-arid grassland in a wet and a dry year in Hungary. *Agr. Ecosyst. Environ. 121*, 21–29.

Pintér, K., Barcza, Z., Balogh, J., Czóbel, Sz., Csintalan, Zs., Tuba, Z. and *Nagy, Z.*, 2008: Interannual variability of grasslands' carbon balance dependson soil type. *Community Ecol. 9* (Suppl.): 43–48.

van den Pol-van Dasselaar, A., van Beusichem, M.L. and *Onema, O.*, 1998: Effects of soil moisture content and temperature on methane uptake by grasslands on sandy soils. *Plant Soil 204,* 213–222.

Priemé, A. and *Christensen, S.*, 2001: Natural perturbations, drying-wetting and freezing-thawing cycles, and the emission of nitrous oxide, carbon dioxide and methane from farmed organic soils. *Soil Biol. Biochem. 33,* 2083–2091.

Reich, P.B., Hobbie, S.E., Lee, T., Ellsworth, D.S., West, J.B., Tilman, D., Knops, J.M.H., Naeem, S. and *Trost, J.*, 2006: Nitrogen limitation constrains sustainability of ecosystem response to CO_2, *Nature* 440, 922–925.

Schimel, D., Braswell, B., McKeown, R., Ojima, D., Parton, W. and. *Pulliam, W.*, 1996: Climate and Nitrogen controls on the geography and timescales of terrestrial biogeochemical cycling. *Global Biogeochem. Cycles 10*, 677–692.

Schindlbacher, A., Zechmeister-Boltenstern, S. and *Butterbach-Bahl, K.*, 2004: Effect of soil moisture and temperature on NO, NO_2, and N_2O emissions from European soils. *J. Geophys. Res. 109*, D17302.

Skiba, U., Drewer, J., Tang, Y.S., van Dijk, N., Helfter, C., Nemitz, E., Famulari, D., Cape, J.N., Jones, S.K., Twigg, M., Pihlatie, M., Vesala, T., Larsen, K.S., Carter, M.S., Ambus, P., Ibrom, A., Beier, C., Hensen, A., Frumau, A., Erisman, J.W., Brüggemann N., Gasche, R., Butterbach-Bahl, K., Neftel, A., Spirig, C., Horvath, L., Freibauer, A., Cellier, P., Laville, P., Loubet, B., Magliulo, E., Bertolini, T., Seufert, G., Andersson, M., Manca, G., Laurila, T., Aurela, M., Lohila, A., Zechmeister-Boltenstern, S., Kitzler, B., Schaufler, G., Siemens, J., Kindler, R., Flechard, C. and *Sutton, M.A.*, 2009: Biosphere–atmosphere exchange of reactive nitrogen and greenhouse gases at the NitroEurope core flux measurement sites: Measurement strategy and first data sets. *Agr. Ecosyst. Environ. 133,* 139–149.

Smith, K.A., Thomson, P.E., Layton, H., McTaggart, I.P. and *Conen, F.*, 1998: Effects of temperature, water content and nitrogen fertilization on emission of nitrous oxide by soils. *Atmos. Environ. 32,* 3301–3309.

Smith, K.A., Ball, T., Conen, F., Dobbie, K.E., Massheder, J. and *Rey, A.*, 2003: Exchange of greenhouse gases between soil and atmosphere: interactions of soil physical factors and biological processes. *European Journal of Soil Science 54,* 779–791.

Soussana, J.F. and *Hartwig, U.A.*, 1996: The effects of elevated CO_2 on symbiotic N_2 fixation: A link between carbon and nitrogen cycles in grassland ecosystems. *Plant Soil 187,* 321–332.

Internet sources:
http://www.met.hu/eghajlat/visszatekinto/elmult_evszazad/

IDŐJÁRÁS

Quarterly Journal of the Hungarian Meteorological Service
Vol. 115, No. 4, October–December 2011, pp. 233–245

Integration of meteo-climatic and remote sensing information for the analysis of durum wheat quality in Val d'Orcia (Tuscany, Italy)

Simone Orlandini[*1], **Marco Mancini**[1], **Grifoni Daniele**[2], **Francesca Orlando**[1], **Anna Dalla Marta**[1], and **Valerio Capecchi**[2]

[1]*Department of Plant, Soil and Environmental Science, University of Florence Piazzale delle Cascine 18, 50144 Florence, Italy*

[2]*CNR–Institute of Biometeorology, Via Caproni 8, 50145 Florence, Italy*

[*]*Corresponding author; E-mail: simone.orlandini@unifi.it*

(Manuscript received in final form May 13, 2011)

Abstract—Climatic and weather conditions largely affect agricultural activities, modifying plant responses and determining the quantity and quality of products. In this respect, the aim of this research was to analyze the quality of winter durum wheat (*Triticum turgidum L. var. durum*) in terms of protein content (%) and test weight through the combined use of meteorological information from ground stations and remote sensing. Meteorological conditions were described using both temperature and precipitation from ground weather stations and the North Atlantic Oscillation (NAO) index. The spectral index used for monitoring the crop was the Normalized Difference Vegetation Index (NDVI). The analysis was carried out for the period 1999–2009 in Tuscany, Central Italy.

Air temperature of the period from February to June was positively correlated with grain protein concentration, while test weight showed negative correlations to temperature in March and May and for all multi-monthly periods starting from March onward. Grain protein concentration appeared as negatively correlated with precipitation cumulated during the entire period from November to June, while no significant effect was observed in test weight. With regard to the NAO, higher correlations to protein content were found for the monthly values of November and February, but more significant results were obtained by aggregating NAO index on a multi-monthly basis when November and February were included. On the other hand, the correlations were negative between the winter NAO index and the specific weight mainly in February and for the period from February to March. Finally, NDVI starting from mid May showed to be negatively related to protein content and positively to test weight. These results demonstrated that precipitation and air temperature over the production area represent

two crucial variables affecting growth and development of winter durum wheat. On the other hand, the use of large-scale meteorological information and specific spectral indices showed a great possibility in the perspective of a local quality forecast system setup.

Key-words: Triticum durum, protein content, specific weight, meteorological information, Normalized Difference Vegetation Index (NDVI), North Atlantic Oscillation index (NAO)

1. Introduction

Cereals are a key product of Italian agriculture, both in terms of direct annual consumption and of the food processing industry's demand. In 2009, Italian wheat production was 6.3 million tons, making it the second most-produced cereal after maize (7.9 million tons; *EUROSTAT*, 2010). In particular, winter durum wheat (*Triticum turgidum L. var. durum*) represents approximately 40% of cultivated wheat of area of production (*EUROSTAT*, 2010). In fact, winter durum wheat provides the raw material for the pasta industry, and a progressively higher amount is also required for the production of special breads, typical products of the southern part of the country. For these reasons, the effect of weather patterns on winter durum wheat is of primary interest. Due to the water shortage and climatic adversities characterizing the cultivation areas, the qualitative and quantitative planning of production is very uncertain and represents an important challenge (*MIPAAF*, 2009).

Most of winter durum wheat in Italy is sown in November and harvested at the beginning of July of the following year. The stem elongation phase starts in April, when the average temperature is 10–12 °C, while ripening starts when the average temperature reaches 18–20 °C. Shooting, grain filling, and grain ripening are the most important development phases that determine the final quality of the grains, so that weather conditions during these periods are crucial for determining the characteristics of production *(Paredes-Lopez et al.*, 1985; *Ciaffi et al.*, 1996).

Several studies confirmed that meteorological factors strongly affect wheat cultivation, by modifying plant responses and determining the final yield and the quality of production.

In general, meteorological variables such as temperature (*Benzian* and *Lane*, 1986; *Smith* and *Gooding*, 1999; *Daniel* and *Triboi*, 2000), sunshine (*Spiertz*, 1977), and rainfall (*Hopkins*, 1968; *Faridi* and *Finley*, 1989; *Bassett et al.*, 1989; *Powlson et al.*, 1992) during grain filling can largely affect the specific weight, the protein content and its composition of wheat grains, as well as the final yield. In UK, the specific weight of wheat grains was correlated negatively with summer precipitation and positively with cumulative sunshine (*Kettlewell et al.*, 2003; *Atkinson et al.*, 2008).

In Australia, the cumulated precipitation during the period from May to September is negatively associated with grain protein content (*Correll et al.*,

1994), while rising temperature after anthesis may increase the grain nitrogen concentration (*Kolderup*, 1975; *Sofield et al.*, 1977). While spring temperature exceeding 30 °C may increase the protein content (*Pan et al.*, 2006), heat stress can cause a reduction of kernel weight and diameter (*Labuschagne et al.*, 2009).

The use of large-scale climatic variables has also been investigated in order to forecast agricultural yields and product quality in several regions of the world (*Atkinson et al.*, 2005). Among these variables and indices that identify the large-scale distribution of air pressure and temperature over defined geographical areas, the Sea Surface Temperature (SST), the El Nino Southern Oscillation (ENSO), and the North Atlantic Oscillation (NAO) are the most studied due to their significant impact on the climate of important production regions worldwide. In Spain, *Gimeno et al.* (2002) found that the yields of many crops (lemon, orange, tangerine, wheat, rye, and olive) were affected by the variations of ENSO and NAO, while in Italy, the effect of NAO, together with 500 hPa geopotential height and SST were related to the quality of wine and durum wheat (*Grifoni et al.*, 2006; *Dalla Marta et al.*, 2010). Many studies demonstrated a relationship between the wheat grain quality (Hagberg falling number, specific weight, and protein concentration) and the winter NAO in the UK (*Kettlewell et al.*, 1999; *Wanner et al.*, 2001; *Hurrell et al.*, 2003; *Atkinson et al.*, 2005; *Atkinson et al.*, 2008). According to *Kettlewell et al.* (2003), the winter NAO has an effect on cumulated precipitation during summer in England and Wales and, consequently, on wheat quality, while *Colman* (1997) suggested an association between SST and NAO in the UK.

Beside the use of meteorological information and numerical model outputs, numerous studies have related to various vegetation indices, of which the normalized difference vegetation index (NDVI) is the most widespread, with crop vigour and biomass (*Filella* and *Penuelas*, 1994; *Broge* and *Lebance*, 2001). Optical remote sensing data have also been used to predict quantitative performances of crops, such as grain yield (*Labus et al.*, 2002; *Singh et al.*, 2002) and biomass production (*Filella* and *Penuelas*, 1994; *Broge* and *Lebance*, 2001). In particular, NOAA-AVHRR NDVI data were related to wheat yield over Italy (*Rossini* and *Benedetti*, 1993) and used for wheat yield estimation over North Africa (*Maselli* and *Rembold*, 2001). Other studies integrated the remote sensing data with crop simulation models for the assessment of crop yield at a regional scale (*Moriondo et al.*, 2007).

On the other hand, there are a few reports on forecasting grain quality, such as protein content, from optical remote sensing data (*Hansen et al.*, 2002; *Basnet et al.*, 2003; *Liu et al.*, 2006).

The main objective of this paper is to analyze the effectiveness of the combined use of large-scale meteorological information and remote sensing imagery, freely available on internet, in analyzing and predicting the winter durum wheat quality in Tuscany (Central Italy).

2. *Materials and methods*

The research was carried in Val d'Orcia, a large region of central Italy (Tuscany), where winter durum wheat is considered an important quality production, and about 15% of the total cultivated surface is allotted to this crop. The study area is characterized by a typical Mediterranean climate, mainly affected by the Azores and Russian anticyclones and by Mediterranean depressions, with a mean annual temperature of about 13.6 °C and a cumulated precipitation of 715 mm, mostly distributed during winter and autumn.

The characteristics of winter durum wheat taken into consideration were the protein content and test weight, mainly related to the production of good quality pasta, to the economics of grain transport, and to milling characteristics.

Data of grain protein content (%) and test weight (kg hl^{-1}) were supplied by the Consorzio Agrario di Siena for the period 1999–2009. Wheat varieties used for this study had similar characteristics and, during the period analyzed, nitrogen fertilization and crop management remained constant. In particular, the fertilization applied was the standard one for the study area with 160 kg ha^{-1} of nitrogen applied in three times and 90 kg ha^{-1} of P_2O_5 applied before sowing. The soil was clay loam.

Air temperature and precipitation (years 1999–2009) were supplied as the mean of five ground stations, in order to most accurately represent the mean meteorological conditions of the production area.

Moreover, the NAO index was used. The NAO is a large-scale mode of natural climate variability that has an important impact on the weather and climate of the North Atlantic region and surrounding continents, especially Europe. The NAO can be described as a temporal fluctuation of the zonal wind strength across the Atlantic Ocean due to pressure variations in both the subtropical anticyclone belt and the subpolar low near Iceland. It is particularly important in winter (December–March), when it exerts a strong control over the climate of the Northern Hemisphere showing a significant relationship with storm track, temperature, and precipitation (*Hurrell* and *van Loon*, 1997). The strength of the NAO is described by the NAO index. It is traditionally defined as the normalized pressure difference between a station in the Azores and one in Iceland. An extended version of the index can be obtained for the winter half of the year by using a station in the southwestern part of the Iberian Peninsula (*Hurrell*, 1995). *Jones et al.* (1997) used early instrumental data to extend the NAO index calculated from Gibraltar and Iceland back to 1823. In this study, we used this last version of the index (http://www.cru.uea.ac.uk/). The NAO index varies from year to year, but also exhibits a tendency to remain in one phase (positive or negative) for intervals lasting several years.

The NDVI was calculated using satellite data derived from the AVHRR sensor. The imagery, downloaded from the website "Free vegetation products" (http://www.free.vgt.vito.be) for the period from November 1988 to June 2009,

were acquired by the satellite SPOT (Satellite Pour l'Observation de la Terre). The spatial resolution was about 1 km × 1 km and time resolution was ten days.

All the considered variables were correlated to wheat protein content and specific weight on a monthly and multi-monthly basis, and all possible combinations were investigated in order to identify the periods during which each variable or index is mainly able to affect or predict the final quality.

Moreover, stepwise multiple regressions between winter durum wheat quality data and the best single descriptors were applied in order to identify the best predictive model (SPSS 15.0).

3. Results and discussion

Individual, monthly air temperature levels were not significantly correlated with protein content, however, persistent positive correlations were observed from February to June with the highest values for April followed by May and June, respectively. The multi-monthly analysis showed significant positive correlations between protein content and air temperature observed from spring to early summer (*Fig. 1*). Concerning specific weight, negative correlations were significant in March and May and for all multi-monthly periods including March (*Fig. 2*).

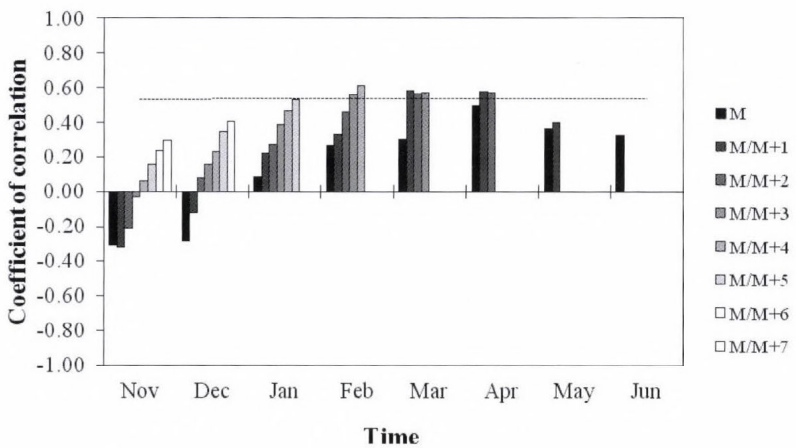

Fig. 1. Coefficient of correlation between protein content at the harvest and air temperature of the preceding single months listed in x axis (*M*) and of the multi-monthly periods starting from each month (*M*) and ending in one of the following months (*M*+1,...,*M*+*n*). Dotted line represents the critical values of *r* for statistical significance at $P \leq 0.05$.

The positive effect of temperature, mainly spring-summer temperature on protein concentration is well known (*Benzian* and *Lane*, 1986; *Gooding* and

Davies, 1977; *Motzo et al.*, 2007). The duration of grain filling in wheat is strongly affected by temperature during this phase (*Wheeler et al.*, 1996) and smaller grains are often resulted from high temperature conditions because, even if the rate of grain growth is increased, this does not compensate for the reduced duration of grain growth. This effect of high temperature penalizes the accumulation of total carbohydrate, thus increasing the relative protein content and decreasing the test weight because of the final grain size and shape; and hence, the degree of dilution of accumulated nitrogen is closely related to the length of time the crop stays green after flowering (*Spiertz*, 1977; *Smith* and *Gooding*, 1999).

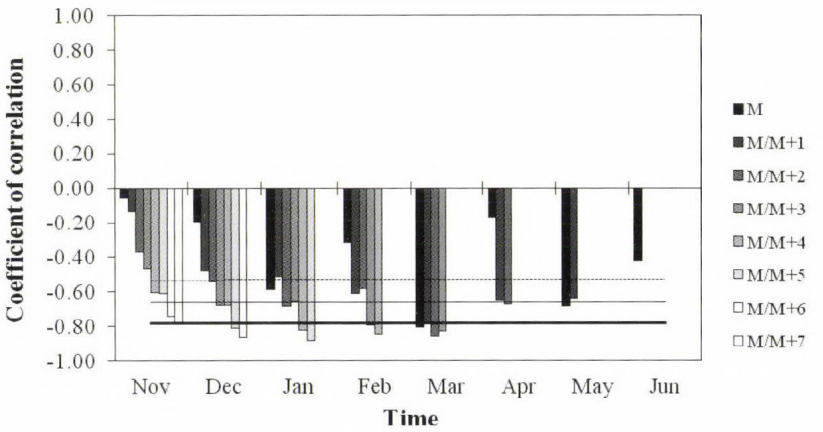

Fig. 2. Coefficient of correlation between specific weight at the harvest and air temperature of the preceding single months listed in x axis (M) and of the multi-monthly periods starting from each month (M) and ending in one of the following months ($M+1, \ldots, M+n$). Dotted line, thin and marked solid lines represent the critical values of r for statistical significance at $P \leq 0.05$, $P \leq 0.01$, and $P \leq 0.001$, respectively.

Monthly precipitation was negatively correlated with protein concentration for the entire period from November to May. The higher and significant correlations were observed for November and April. The multi-monthly analysis showed a more complex situation, where significant negative correlations were mainly observed for periods including November (all the periods starting from November up to the end of the growing season) and April (*Fig. 3*). No significant correlation was found between rainfall and specific weight (data not shown), although other studies, carried on in the UK on wheat, showed a negative effect of precipitation during grain filling, mainly due to the alternate wetting and drying causing wrinkling of the grain surface (*Kettlewell et al.*, 2003; *Atkinson et al.*, 2008).

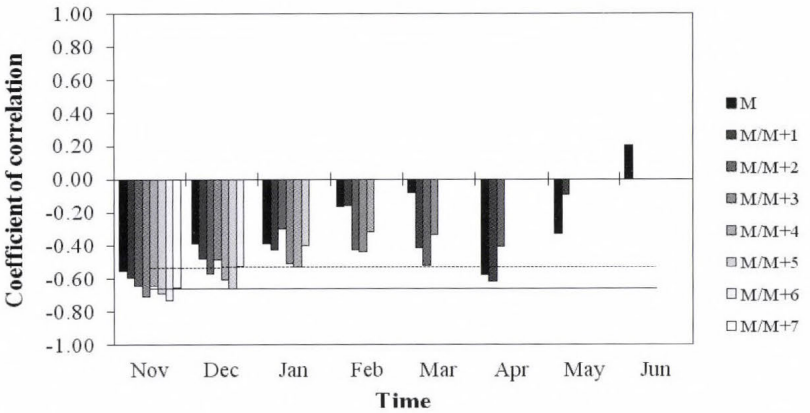

Fig. 3. Coefficient of correlation between protein content at the harvest and cumulated rainfall of the preceding single months listed in x axis (*M*) and of the multi-monthly periods starting from each month (*M*) and ending in one of the following months ($M+1,...,M+n$). Dotted and solid lines represent the critical values of r for statistical significance at $P \leq 0.05$ and $P \leq 0.01$, respectively

Rainfall and soil water availability reduces protein content because they enhance dilution of early nitrogen reserves by vegetative proliferation; it increases leaching and other forms of soil nitrogen losses and it may augment soil moisture reserves so that leaf life is extended during grain growth, favouring carbohydrate assimilation and translocation more than that of nitrogen; thus, a yield increase corresponds to a reduction in protein concentration (*Schlehuber* and *Trucher*, 1959; *Hopkins*, 1968; *Taylor* and *Gilmour*, 1971; *Smith* and *Gooding*, 1999; *Oweis et al.*, 1999).

As far as the NAO is concerned, winter durum wheat quality was positively correlated with the index several months, in particular during the winter period. Higher correlations on a monthly basis were found for November and February, and more significant results were obtained by aggregating the NAO index on a multi-monthly basis when November and February were included (*Fig. 4*). On the contrary, the correlations were negative between the winter NAO index and specific weight, mainly the index of February and for the period January–March (*Fig. 5*).

This result can be explained by the winter NAO index defining a specific atmospheric synoptical configuration over the Atlantic Ocean, affecting winter precipitation and winter and early spring temperatures over the Mediterranean sea and consequently over the study area (*Hurrel* and *van Loon*, 1997; *Bartolini et al.*, 2009). Winter durum wheat protein and specific weight were slightly stronger correlated with the NAO index than with cumulated precipitation and temperature, respectively, probably because the NAO index is able to better describe the environmental conditions (being a consequence of atmospheric circulation) rather than a single meteorological variable.

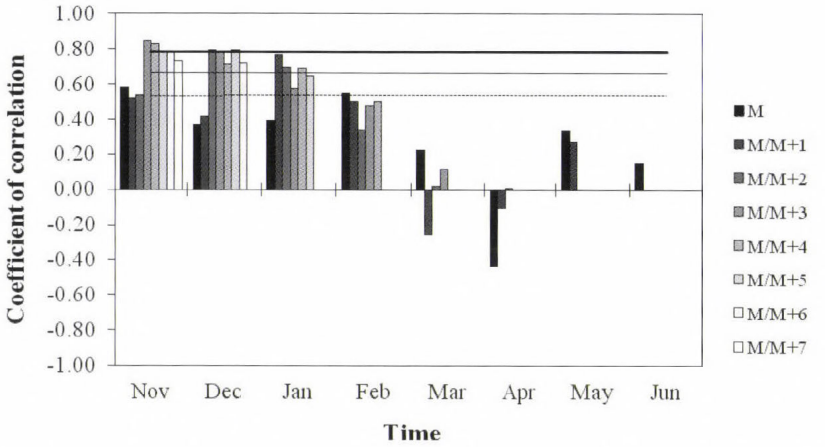

Fig. 4. Coefficient of correlation between protein content at the harvest and the NAO Index of the preceding single months listed in x axis (*M*) and of the multi-monthly periods starting from each month (*M*) and ending in one of the following months (*M*+1,...,*M*+*n*). Dotted line, thin and marked solid lines represent the critical values of *r* for statistical significance at $P \leq 0.05$, $P \leq 0.01$, and $P \leq 0.001$, respectively.

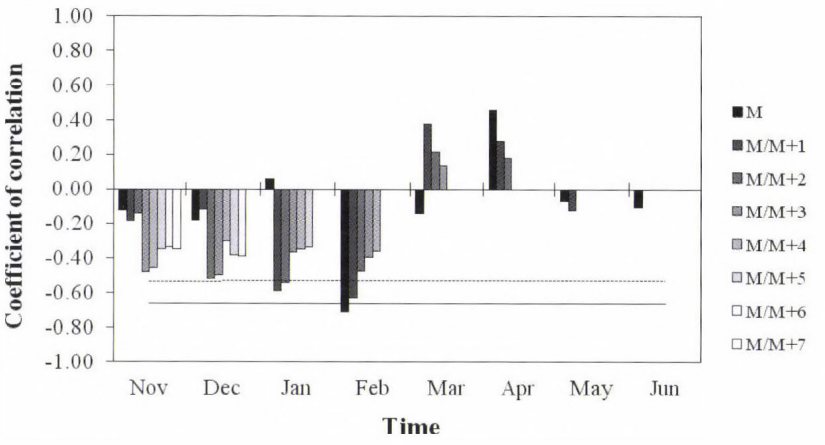

Fig. 5. Coefficient of correlation between specific weight at the harvest and the NAO Index of the preceding single months listed in x axis (*M*) and of the multi-monthly periods starting from each month (*M*) and ending in one of the following months (*M*+1,...,*M*+*n*). Dotted and solid lines represent the critical values of *r* for statistical significance at $P \leq 0.05$ and $P \leq 0.01$, respectively.

NDVI was significantly correlated with durum wheat quality parameters, negatively with protein content and positively with specific weight, starting from mid May to the end of the season (*Tables 1* and *2*).

Table 1. Coefficient of correlation (r) between wheat protein content at harvest and NDVI for decadal and multi-decadal periods. The number after the month indicates the decade considered. Critical values of r for statistical significance are: $r \geq 0.576$, $P \leq 0.05^{*}$; $r \geq 0.708$, $P \leq 0.01^{**}$

Apr3	**Apr3–May1**	**Apr3–May2**	**Apr3–May3**	**Apr3–Jun1**	**Apr3–Jun2**	**Apr3–Jun3**
0.132	0.108	0.023	–0.303	–0.432	–0.665*	–0.685*
May1	**May1–May2**	**May1–May3**	**May1–Jun1**	**May1–Jun2**	**May1–Jun3**	
0.017	–0.106	–0.515	–0.646*	–0.726**	–0.735**	
May2	**May2–May3**	**May2–Jun1**	**May2–Jun2**	**May2–Jun3**		
–0.190	–0.428	–0.700*	–0.768**	–0.775**		
May3	**May3–Jun1**	**May3–Jun2**	**May3–Jun3**			
–0.787**	–0.425	–0.440	–0.443			
Jun1	**Jun1–Jun2**	**Jun1–Jun3**				
–0.606*	–0.766**	–0.774**				
Jun2	**Jun2–Jun3**					
–0.783**	–0.772**					
Jun3						
–0.667*						

Table 2. Coefficient of correlation (r) between wheat specific weight at harvest and NDVI for decadal and multi-decadal periods. The number after the month indicates the decade considered. Critical values of r for statistical significance are: $r \geq 0.576$, $P \leq 0.05^{*}$; $r \geq 0.708$, $P \leq 0.01^{**}$; $r \geq 0.823$, $P \leq 0.001^{***}$

Apr3	**Apr3–May1**	**Apr3–May2**	**Apr3–May3**	**Apr3–Jun1**	**Apr3–Jun2**	**Apr3–Jun3**
0.184	0.312	0.417	0.689*	0.722**	0.771**	0.731**
May1	**May1–May2**	**May1–May3**	**May1–Jun1**	**May1–Jun2**	**May1–Jun3**	
0.350	0.576*	0.836***	0.717**	0.744**	0.708**	
May2	**May2–May3**	**May2–Jun1**	**May2–Jun2**	**May2–Jun3**		
0.501	0.693*	0.665*	0.713**	0.686*		
May3	**May3–Jun1**	**May3–Jun2**	**May3–Jun3**			
0.845***	0.782**	0.735**	0.695*			
Jun1	**Jun1–Jun2**	**Jun1–Jun3**				
0.376	0.593*	0.584*				
Jun2	**Jun2–Jun3**					
0.700*	0.633*					
Jun3						
0.466						

Protein concentration is often closely related to wheat yield, that is the parameter most widely monitored and predicted by the use of NDVI. Typically, wheat is fertilized during seeding to meet a specific yield and/or protein concentration potential based on available information on soil fertility, water holding capacity, and expected growing season rainfall (*Selles* and *Zentner*, 1998). If growing conditions are more favorable than anticipated, strong early growth of the crop will deplete soil nutrients leaving little for the critical grain filling period in wheat. This can often result in a high yield but lower protein concentration than desired. Thus, there is a common inverse relationship between wheat yield and protein concentration (*Siman*, 1974). For the same reason, a positive correlation was found between NDVI and specific weight.

The final step of this study was to evaluate the effect of all the considered variables as a whole by means of a stepwise linear multiple regression analysis. The model, based on an automatic procedure of variable inclusion/exclusion was tested by using the multi-monthly periods for which the best correlation coefficients were obtained for each single variable previously analyzed. In particular, for protein content the variables used were February–June air temperature, November–May precipitation, November–February NAO, and NDVI of the third decade of May. For the specific weight, the variables used were February NAO, January–June temperature, and NDVI of the third decade of May. In the first case, within the stepwise regression results, the simplest model was obtained using NAO index (R^2=0.822), while the addition of temperature gave the best-fit model and resulted in an R^2 of 0.905. Precipitation and NDVI were excluded, since their addition to the model failed to improve its performance. Concerning specific weight, the simplest and best-fit model was obtained using temperature data (R^2=0.781), while the other variables considered where excluded.

4. Conclusions

This paper investigates relations between climatic and weather conditions, information derived from remote sensing data and the quality of winter durum wheat cultivated in Val d'Orcia. The results demonstrated that precipitation and temperature over the production area represent two crucial variables, which drive the vegetative and productive responses of wheat. On the other hand, the use of large-scale meteorological information showed a great possibility. In fact, the correlation existing between the NAO index, partially determining the distribution of temperature and precipitation over the study area, and winter durum wheat protein content, seems to provide a great deal of information which is capable of summarizing the effect of climate on the qualitative characteristics. This assumption was confirmed by the multiple regression model that selected the NAO index and temperature as the best predictors of the final grain quality. On the other hand, also the analysis of NDVI showed its crucial

importance for predicting the final quality. In fact, already starting from May, about one month before the harvest, this index was strongly correlated to both quality characteristics considered. Moreover, indices derived from remote sensing have the advantage to well represent the spatial variability of the observed parameters.

For analyzing the effect of climate on winter durum wheat quality on the long term, the application of crop growth simulation models is desirable in order to create datasets that are unaffected by particular trends due to technological development or variety improvement. Then, the use of high resolution satellite imagery has to be analyzed for the monitoring of the crop at farm level.

Significant future applications of this knowledge are possible by the development of specific forecast tools. In fact, the analysis of such meteorological variables during specific times could be used to forecast the winter durum wheat quality of the following production with a certain level of accuracy. Moreover, the possibility of using meteorological information freely available on internet can reduce costs and spatial and temporal representativeness limitations related to weather monitoring in loco.

The importance of the above described studies is mostly related to the potential development of a winter durum wheat local quality forecast system in order to provide cereal growers, technicians and pasta producers with useful information on the potential quality of the following production. The integration of these results with operational climatic seasonal forecasts may, in fact, represent the basis of a provisional quality system to support the winter durum wheat production sector.

Acknowledgments—The authors wish to thank *Fondazione Monte dei Paschi di Siena* and *Consorzio Agrario di Siena*, for their support to this research, and *Federico Guasconi* for his help in data processing.

References

Atkinson, M.D., Kettlewell, P.S., Poulton, P.R. and *Hollins, P.D.*, 2008: Grain quality in the Broadbalk wheat experiment and the winter North Atlantic Oscillation. *J. Agric. Sci. 146*, 541–549.

Atkinson, M.D., Kettlewell, P.S., Hollins, P.D., Stephenson, D.B., and *Hardwik, N.V.*, 2005: Summer climate mediates UK wheat quality response to winter North Atlantic Oscillation. *Agr. Forest Meteorol. 130*, 27–37.

Bartolini, E., Claps, P. and *D'Odorico, P.*, 2009: Interannual variability of winter precipitation in the European Alps: relations with the North Atlantic Oscillation. *Hydrol. Earth Syst. Sci. 13*, 17–25.

Basnet, B., Apan, A., Kelly, R., Jensen, T., Strong, W. and *Butler, D.*, 2003: Relating satellite imagery with grain protein content of grain crops. *Proceedings of the Spatial Sciences Conference*, Canberra, Australia (CD–ROM), 22–27.

Bassett, L.M., Allen, R.E. and *Rubenthaler, G.L.*, 1989: Genotype × environment interactions on soft white winter wheat quality. *Agron J. 81*, 955–960.

Benzian, B. and *Lane, P.W.*, 1986: Protein concentration of grain in relation to some weather and soil factors during 17 years of English winter-wheat experiments. *J. Sci. Food Agric. 37*, 435–444.

Broge, N.H. and *Lebance, E.*, 2001: Comparing prediction power and stability of broadband and hyperspectral vegetation indices for estimation of green leaf area index and canopy chlorophyll density. *Remote Sens. Environ. 76*, 156–172.

Ciaffi, M., Tozzi, L., Borghi, B., Corbellini, M. and *Lafiandra, D.*, 1996: Effect of heat shock during grain filling on the gluten protein composition of bread wheat. *J. Cereal Sci. 24*, 91–100.

Colman, A., 1997: Prediction of summer central England temperature from preceding North Atlantic winter sea surface temperature. *Int. J. Climatol. 17*, 1285–1300.

Correll, R., Butler, J., Spouncer, L. and *Wrigley, C.*, 1994: The relationship between grain-protein content of wheat and barley and temperatures during grain filling. *Aus. J. Plant Physiol. 21*, 869–873.

Dalla Marta, A., Grifoni, D., Mancini, M., Zipoli, G. and *Orlandini, S.*, 2010: The influence of climate on durum wheat quality in Tuscany, Central Italy. *Int. J. Biometeorol. DOI: 10.1007/s00484-010-0310-8.*

Daniel, C. and *Triboi, E.J.*, 2000: Effects of temperature and nitrogen nutrition on the grain composition of winter wheat: effects on gliadin content and composition. *J. Cereal Sci. 32*, 45–56.

Faridi, H. and *Finley, J.W.*, 1989: Improved wheat for baking. *CRC Crit. Rev. Food Sci. and Nutr. 28*, 175–209.

Filella, I. and *Peñuelas, J.*, 1994: The red edge position and shape as indicators of plant chlorophyll content, biomass and hydric status. *Int. J. Remote Sens. 15*, 1459–1470.

Gimeno, L., Ribera, P., Iglesias, R., de la Torre, L., Garcia, R. and *Hernandez, E.*, 2002: Identification of empirical relationships between indices of ENSO and NAO and agricultural yields in Spain. *Clim. Res. 21*, 165–172.

Gooding, M.J. and *Davies, W.P.*, 1997: Wheat production and utilization: systems, quality and the environment. *CAB International*, Wallingford, UK.

Grifoni, D., Mancini, M., Maracchi, G., Orlandini, S. and *Zipoli, G.*, 2006: Analysis of Italian wine quality using freely available meteorological information. *Am. J. Enol. Vitic. 57*, 339–346.

Hansen, P., Jørgensen, J.R. and *Thomsen, A.*, 2002: Predicting grain yield and protein content in winter wheat and spring barley using repeated canopy reflectance measurements and partial least squares regression. *J. Agric. Sci. 139*, 307–318.

Hopkins, J.W., 1968: Protein content of western Canadian hard red spring wheat in relation to some environmental factors. *Agr. Meteorol. 5*, 411–431.

Hurrell, J.W., 1995: Decadal trends in the North Atlantic Oscillation and relationships to regional temperature and precipitation. *Science 269*, 676–679.

Hurrel, J.W. and *van Loon, H.*, 1997: Decadal variations in climate associated with the North Atlantic Oscillation. *Climatic Change 36*, 301–326.

Hurrell, J.W., Kushnir, Y., Ottersen, G. and *Visbeck, M.*, 2003: An Overview of the North Atlantic Oscillation. In *The North Atlantic Oscillation: Climate Significance and Environmental Impact* (eds.: *J.W. Hurrell, Y. Kushnir, G. Ottersen,* and *M. Visbeck*). Geophysical Monograph Series 134, 1–36.

Jones, P.D., Jonsson, T. and *Wheeler, D.*, 1997: Extension to the North Atlantic Oscillation using early instrumental pressure observations from Gibraltar and South-West Iceland. *Int. J. Climatol. 17*, 1433–1450.

Jones, P.D., Osborn, T.J. and *Briffa, K.R.*, 1997: Estimating sampling errors in large-scale temperature averages. *J. Climate 10*, 2548–2568.

Kettlewell, P.S., Sothern, R.B. and *Koukkari, W.L.J.*, 1999: U.K. wheat quality and economic value are dependent on the North Atlantic Oscillation. *J. Cereal Sci. 29*, 205–209.

Kettlewell, P.S., Stephenson, D.B., Atkinson, M.D. and *Hollins, P.D.*, 2003: Summer rainfall and wheat grain quality: relationships with the North Atlantic Oscillation. *Weather 58*, 155–164.

Kolderup, F., 1975: Effects of temperature, photoperiod and light quantity on protein production in wheat grains. *J. Sci. Food and Agric. 26*, 583–592.

Labus, M.P., Nielsen, G.A., Lawrence, R., Engel, R. and *Long, D.S.*, 2002: Wheat yield estimates using multi-temporal NDVI satellite imagery. *Int. J. Remote Sens. 23*, 4169–4180.

Labuschagne, M.T., Elago, O. and *Koen, E.J.*, 2009: The influence of temperature extremes on some quality and starch characteristics in bread, biscuit and durum wheat. *J. Cereal Sci. 49*, 184–189.

Liu, L., Wang, J., Bao, Y., Huang, W., Ma, Z. and *Zhao C.*, 2006: Predicting winter wheat condition, grain yield and protein content using multi-temporal EnviSat-ASAR and Landsat TM satellite images. *Int. J. Remote Sens. 27*, 737–753.

Maselli, F. and *Rembold, F.*, 2001: Analysis of GAC NDVI data for cropland identification and yield forecasting in Mediterranean African countries. *Photogramm. Eng. Rem. S. 67*, 593–602.

Moriondo, M., Maselli, F. and *Bindi, M.*, 2007: A simple model of regional wheat yield based on NDVI data. *Eur. J. Agron. 26*, 266–274.

Motzo, R., Fois, S. and *Giunta, F.*, 2007: Protein content and gluten quality of durum wheat (*Triticum turgidum subsp. durum*) as affected by sowing date. *J. Sci. Food Agric. 87*, 1480–1488.

Oweis, T., Pala, M. and *Ryan, J.*, 1999: Management alternatives for improved durum wheat production under supplemental irrigation in Syria. *Eur. J. Agron. 11*, 255–266.

Pan, J., Zhu, Y., Cao, W., Dai, T. and *Jiang, D.*, 2006: Predicting the protein content of grain in winter wheat with meteorological and genotypic factors. *Plant Prod. Sci. 9*, 323–333.

Paredes-Lopez, O., Corravioubas-Alvarez, M. and *Barquin-Carmona, J.*, 1985: Influence of nitrogen fertilization on the physicochemical and functional properties of bread wheats. *Cereal Chem. 62*, 427–432.

Powlson, D.S., Hart, P.B.S., Poulton, P.R., Johnston, A.E. and *Jenkinson, D.S.*, 1992: Influence of soil type, crop management and weather on the recovery of 15N-labelled fertilizer applied to winter wheat in spring. *J. Agric. Sci. 118*, 83–100.

Rossini, P. and *Benedetti, R.*, 1993: On the use of NDVI profiles as a tool for agricultural statistics: the case study of wheat yield estimate and forecast in Emilia Romagna. *Remote Sens. Environ. 45*, 311–326.

Schlehuber, A.M. and *Tucker, B.B.*, 1959: Factors affecting the protein content of wheat. *Cereal Sci. Today 4*, 240–242.

Selles, F. and *Zentner, R.P.*, 1998: Environmental factors affecting wheat protein. In *Proceedings of the Wheat Protein Symposium on Production and Marketing* (eds.: *D.B. Fowler, W.E. Geddes, A.M. Johnston,* and *K.R. Preston*). University of Saskatchewan, Saskatoon, Canada, 139–1150.

Siman, G., 1974: Nitrogen status in growing cereals. *PhD Thesis of The Royal Agricultural College of Sweden*, Uppsala.

Singh, R., Semwal, D.P., Rai, A. and *Chhikara, R.S.*, 2002: Small area estimation of crop yield using remote sensing satellite data. *Int. J. Remote Sens. 23*, 49–56.

Smith, G.P. and *Gooding, M.J.*, 1999: Models of wheat grain quality considering climate, cultivar and nitrogen effects. *Agr. Foest. Meteorol. 94*, 159–170.

Sofield, I., Evans, L.T., Cook, M.G. and *Wardlaw, I.F.*, 1977: Factors influencing the rate and duration of grain filling in wheat. *Aust. J. Plant Physiol. 4*, 785–797.

Spiertz, J.H.J., 1977: The influence of temperature and light intensity on grain growth in relation to the carbohydrate and nitrogen economy of the wheat plant. *Neth. J. Agr. Sci. 25*, 182–197.

Taylor, A.C. and *Gilmour, A.R.*, 1971: Wheat protein prediction from climatic factors in southern New South Wales. *Aust. J. Exp. Agr. Anim. Husbandry 11*, 546–549.

Wanner, H., Bronnimann, S., Casty, C., Gyalistras, D., Luterbacher, J., Schmutz, C., Stephenson, D.B. and *Xoplaki, E.*, 2001: North Atlantic Oscillation – Concepts and studies. *Surv. Geophys. 22*, 321–381.

Wheeler, T.R., Hong T.D., Ellis R.H., Batts G.R., Morison J.I.L. and *Hadley P.*, 1996: The duration and rate of grain growth, and harvest index, of wheat (*Triticum aestivum L.*) in response to temperature and CO_2. *J. Exp. Bot. 298*, 623–630.

Internet sources:

EUROSTAT (*Statistical Office of the European Commission*), 2010: http://epp.eurostat.ec.europa.eu/portal/page/portal/eurostat/home/

MIPAAF (Ministero delle Politiche Agricole Alimentari e Forestali), 2009: http://www.politicheagricole.it/default.html

IDŐJÁRÁS

Quarterly Journal of the Hungarian Meteorological Service
Vol. 115, No. 4, October–December 2011, pp. 247–263

Comparative modeling study of the effect of parameterizations based on rime accretion rate and effective water content on the simulated charge density in thunderstorms

Boryana Tsenova[1*] and **Rumjana Mitzeva**[2]

[1] *National Institute of Meteorology and Hydrology,*
Bulgarian Academy of Sciences,
66 Tsarigradsko chaussee, 1784 Sofia, Bulgaria

[2] *Department of Meteorology and Geophysics, Faculty of Physics,*
University of Sofia,
5 James Bourchier Blvd, 1164 Sofia, Bulgaria
E-mail: rumypm@phys.uni-sofia.bg

[*] *Corresponding author; E-mail: boryana.tsenova@meteo.bg*

(Manuscript received in final form May 3, 2011)

Abstract—A new parameterization for non-inductive charging based on the laboratory studies of. *Takahashi* (1978) is proposed that includes the effect of rime accretion rate on the charge transfer. Numerical simulations of two idealized cloud cases are performed to test the effect of parameterizations used in the model on the cloud charge structure. The parameterizations are based on two different sets of well known laboratory experiments applying two different manners of determination of separated charge as a function of the effective water content or the rime accretion rate. Results show that using parameterizations based on the data of *Saunders et al.* (1991) the total charge density is larger in comparison to cases when *Takahashi* based parameterizations are used. Additionally, the different manner of charge determination (as a function of the effective water content or the rime accretion rate) leads to more considerable differences in the cloud charge structure when *Saunders* parameterizations are used, comparing to the cases when *Takahashi* parameterizations are used.

Key-words: non-inductive charging, parameterization, rime accretion rate, effective water content

1. Introduction

It is accepted that thunderstorm electrification is mainly due to non-inductive charging during interactions between ice cloud particles. The non-inductive mechanism of charging is the mechanism known to be capable of generating an electric field of ~100 kV/m in a few minutes. It results from charge separation (independently of external electric fields) during rebounding collision between riming graupel and ice crystals in the presence of supercooled cloud droplets. Many experimental studies (*Takahashi*, 1978; *Jayaratne et al.*, 1983; *Saunders et al.*, 1991; *Takahashi* and *Miyawaki*, 2002; *Saunders et al.*, 2004, and others) were directed to reveal the factors controlling the sign and magnitude of the separated charge. Based on laboratory experiments, it was specified that the sign and the magnitude of the charge transfer during a collision between a riming target simulating a graupel particle and an ice crystal depends on cloud temperature and cloud effective water content determined by the ability of the graupel to capture supercooled water droplets. However, dependencies are different for the various experiments and there is no consensus which laboratory results are more reliable in representing charging in real clouds. Recently, it was assumed (*Pereyra et al.*, 2000; *Saunders et al.*, 2006) that the marked difference in the charge sign reversal lines in the laboratory experiments is due to the type of the laboratory clouds (one-cloud chamber or two-cloud chamber), and that the different results should be used for charge separation in different cloud regions. In numerical models, thunderstorm electrification is calculated using different parameterizations based on the laboratory experiments. Based on their laboratory results, *Saunders et al.* (1991) proposed empirical equations for the sign and magnitude of the separated charge as a function of the effective water content and the temperature. In *Tsenova* and *Mitzeva* (2009), equations for *Takahashi* (1978) laboratory data are proposed to determine the separated charge depending on the cloud temperature and effective water content, to avoid the use of the look-up table data (which is computationally more time-expensive) used in all numerical model studies before.

Based on laboratory measurements and physical considerations *Brooks et al.* (1997) suggested that the rime accretion rate (*RAR*) which includes the effect of the relative velocity of interacting particles on the separated charge, is more appropriate to be used for the determination of the charge transfer than the effective water content. They proposed modifications of the equations in *Saunders et al.* (1991) for the separated charge to be presented as a function of cloud temperature and rime accretion rate.

In the present study, following the idea in *Brooks et al.* (1997) we propose modification of the equations in *Tsenova* and *Mitzeva* (2009) for the charge transfer obtained in *Takahashi* (1978) as a function of the rime accretion rate. Besides introducing a new parameterization of non-inductive charging that uses these equations, the present work is directed to test the difference in the charge

structures as a result of the different parameterizations (based on *Saunders et al.* (1991) or *Takahashi* (1978) laboratory results, or determining the separated charge as a function of the effective water content or the rime accretion rate). Numerical simulations of two cloud cases are carried out with a 1.5-D cloud model. Many authors have performed similar studies with 3-D cloud models (*Helsdon et al.*, 2001; *Mansell et al.*, 2005; *Barthe et al.*, 2007, and others) and their results are certainly more representative for real clouds. However, we believe that such a basic numerical study performed with a 1.5-D cloud model, which is appropriate to simulate the cloud core, would be helpful for a better understanding of the effect of the used scheme for non-inductive charging on thundercloud electrification. It has to be stressed that as it is shown in *Mitzeva et al.* (2009), model-simulated charge structures during growth stages of thunderstorms depend significantly on the particular model used. Thus, using 1.5-D cloud model we do not intend to make conclusions regarding which of the parameterizations are better suited to the realistic simulation of the electrical charging in real clouds.

2. *Parameterization of non-inductive charging*

The revised equations presented here take into account the dependence of the charge transfer on the relative velocity between interacting particles, which was 8 m/s during the laboratory experiments in *Takahashi* (1978). The equations are presented in two forms, involving *EW* (effective water content) or *RAR* (rime action rate); the factor 8 normalizes the results of Takahashi obtained at 8 m/s.

For $T > -10$ °C:

- $\left(EW \times \frac{V}{8}\right) \leq 1.6$ g/(m^{2}s):

$$q_T = 146.981\left(EW \times \frac{V}{8}\right) - 116.37\left(EW \times \frac{V}{8}\right)^2 + 29.762\left(EW \times \frac{V}{8}\right)^3$$
$$- 0.03T^3\left(EW \times \frac{V}{8}\right) - 2.581T - 0.0209T^3\left(EW \times \frac{V}{8}\right)^3 + 0.356T^3\left(EW \times \frac{V}{8}\right)^2, \quad \text{(1a)}$$
$$+ 0.15T^2 + 2.918T\left(EW \times \frac{V}{8}\right)^3 - 4.215T\left(EW \times \frac{V}{8}\right) - 8.5059$$

- $RAR \leq 12.8$ g/(m^{2}s):

$$q_T = 18.37RAR - 1.82RAR^2 + 0.06RAR^3$$
$$- 0.004T^3RAR - 2.581T - 0.0004T^3RAR^3 + 0.006T^3RAR^2, \quad \text{(1b)}$$
$$+ 0.15.T^2 + 0.006TRAR^3 - 0.53TRAR - 8.5059$$

- $\left(EW \times \frac{V}{8}\right) > 1.6$ g/(m^{2}s):

$$q_T = 4.17952T - 0.00452T^2\left(EW \times \frac{V}{8}\right)^2 + 0.91617\left(EW \times \frac{V}{8}\right)^2$$
$$-1.33266T\left(EW \times \frac{V}{8}\right) - 7.46539\left(EW \times \frac{V}{8}\right) + 0.10968T\left(EW \times \frac{V}{8}\right)^2, \quad (2a)$$
$$+0.00057T^2\left(EW \times \frac{V}{8}\right)^3 - 0.03504\left(EW \times \frac{V}{8}\right)^3 + 50.84454$$

- $RAR > 12.8$ g/(m^{2}s):

$$q_T = 4.17952T - 0.00007T^2RAR^2 + 0.01RAR^2$$
$$-017TRAR - 0.93RAR + 0.002TRAR^2 \quad , \quad (2b)$$
$$+0.000001T^2RAR^3 - 0.00007\,RAR^3 + 50.84454$$

For $T \leq -10$°C:

- $\left(EW \times \frac{V}{8}\right) \leq 0.4$ g/(m^{2}s):

$$q_T = -3.3515T + 95.957T\left(EW \times \frac{V}{8}\right)^2 + 511.8315\left(EW \times \frac{V}{8}\right)$$
$$+17.4482T^2\left(EW \times \frac{V}{8}\right)^3 - 0.0007T^3 + 20.5702T\left(EW \times \frac{V}{8}\right)$$
$$+0.1656T^2\left(EW \times \frac{V}{8}\right) + 0.4954T^3\left(EW \times \frac{V}{8}\right)^3 - 0.0975T^3\left(EW \times \frac{V}{8}\right)^2 \quad , \quad (3a)$$
$$+67.4565T\left(EW \times \frac{V}{8}\right)^3 - 0.1066T^2 - 24.5715$$

- $RAR \leq 3.2$ g/(m^{2}s):

$$q_T = -3.3515T + 1.5TRAR^2 + 63.98RAR$$
$$+0.03T^2RAR^3 - 0.0007T^3 + 2.57TRAR \quad , \quad (3b)$$
$$+0.02T^2RAR + 0.001T^3RAR^3 - 0.002T^3RAR^2$$
$$+0.13TRAR^3 - 0.1066T^2 - 24.5715$$

- $0.4\ \text{g/(m}^2\text{s)} < \left(EW \times \frac{V}{8}\right) \leq 3.2\ \text{g/(m}^2\text{s)}$:

$$q_T = -1.5676\,T\left(EW \times \frac{V}{8}\right) + 0.2484\,T\left(EW \times \frac{V}{8}\right)^3 + 0.0112\,T^3$$
$$+ 19.1993\,T + 0.8051\,T^2 + 5.97\left(EW \times \frac{V}{8}\right)^3 - 83.3911\left(EW \times \frac{V}{8}\right), \qquad (4a)$$
$$+ 15.3636\left(EW \times \frac{V}{8}\right)^2 + 167.9278$$

- $3.2\ \text{g/(m}^2\text{s)} < RAR \leq 25.6\ \text{g/(m}^2\text{s)}$:

$$q_T = -0.2TRAR + 0.0005TRAR^3 + 0.0112T^3$$
$$+ 19.1993T + 0.8051T^2 + 0.01RAR^3 - 10.42RAR, \qquad (4b)$$
$$+ 0.24RAR^2 + 167.9278$$

- $\left(EW \times \frac{V}{8}\right) > 3.2\ \text{g/(m}^2\text{s)}$:

$$q_T = 4.212661\,T - 0.83119T\left(EW \times \frac{V}{8}\right) + 0.067005\,T\left(EW \times \frac{V}{8}\right)^2$$
$$+ 0.004245T^2\left(EW \times \frac{V}{8}\right) + 40.96417 \qquad (5a)$$

- $RAR > 25.6\ \text{g/(m}^2\text{s)}$:

$$q_T = 4.212661T - 0.1TRAR + 0.001TRAR^2$$
$$+ 0.0005T^2RAR + 40.96417, \qquad (5b)$$

where q_T is the separated charge in fC,
T is the in-cloud temperature in °C,
EW is the effective water content in g/m^3,
V is the relative velocity between the interacting particles, and
RAR is the rime accretion rate in $\text{g/(m}^2\text{s)}$.

Fig. 1 shows the sign of charge transfer to a riming target during ice crystal collisions at 8 m/s as a function of rime accretion rate and temperature calculated by the Eqs. (1b)–(5b) corresponding to laboratory results (*Takahashi*, 1978; *Takahashi* and *Miyawaki*, 2002).

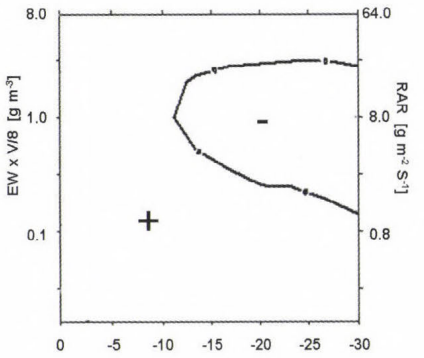

Fig. 1. Sign of the charge transfer to a riming target during ice crystal collisions at 8 m/s obtained by Eqs. (1b)–(5b) corresponding to laboratory results in *Takahashi* (1978) and *Takahashi* and *Miyawaki* (2002), as a function of in-cloud temperature (x axis) and rime accretion rate: $RAR = EW \times V$.

In *Fig. 2* one can see the sign of the charge transfer in EW/T (left panel of *Fig. 2*) and RAR/T (right panel of *Fig. 2*) diagrams according to *Saunders et al.* (1991) and *Brooks et al.* (1997; SKM and BSMP, respectively) and *Takahashi* (1978) (TAK and TRAR, respectively) laboratory results. In EW/T diagram (*Fig. 2*, left panel) the charge sign reversal lines are obtained using the two parameterizations denoted here with SKM and TAK. The SKM parameterization is based on equations presented in *Saunders et al.* (1991) for the non-inductive charge transfer as a function of cloud temperature and effective water content, EW. The TAK parameterization consists of the empirical equations proposed in *Tsenova* and *Mitzeva* (2009) to calculate the charge values of *Takahashi* (1978) at different cloud temperatures and effective water contents.

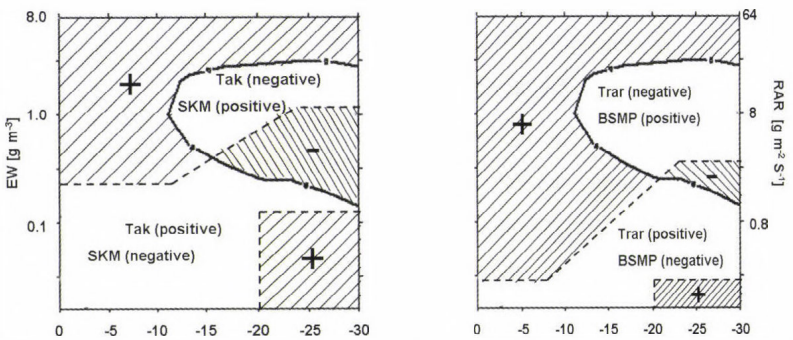

Fig. 2. Charge transfer sign in EW/T (left panel) and RAR/T (right panel) diagrams according to *Saunders et al.*, (1991; SKM and BSMP, respectively) and *Takahashi* (1978; TAK and TRAR respectively) laboratory results, as a function of in-cloud temperature (x axis). Hatching indicates the regions where the charge sign is identical based on both parameterizations, while on non-hatched regions the charge sign is different based on both parameterizations.

From *Fig. 2* one can see the regions where the charge sign is identical based on both parameterizations which are hatched, and the regions where the charge sign is different based on both parameterizations which are not hatched. At low values of EW, the charge transfer according to SKM parameterization is negative, except for the positive charging at temperatures lower than –20 °C (corresponding to the "positive anomaly" in *Saunders et al.* (1991)), while, according to TAK the charge transfer is positive. Conversely, at intermediate and high values of EW and T, according to SKM parameterization, the charge is positive, while according to TAK , it is negative. In RAR/T diagram (*Fig. 2*, right panel), the charge sign reversal lines are obtained using the BSMP and TRAR parameterizations. The BSMP parameterization is represented by a set of the revised equations presented in *Brooks et al.*, (1997) for the non-inductive charge transfer taking into account the effect of rime accretion rate and temperature on the charge transfer to the target during ice crystal collisions at 3 m/s. The anomalous zones are also included (at low EW), presented in *Saunders et al.* (1991), but not considered in *Brooks et al.* (1997). The *TRAR* parameterization is the set of the Eqs. (1b) – (5b). In the RAR/T diagram, the positively charged region according to both parameterizations BSMP and TRAR is larger than the positively charged region according to SKM and TAK in EW/T diagram. Conversely, the negatively charged region according to both parameterizations BSMP and TRAR is narrowed compared to the negatively charged region according to SKM and TAK. At low temperatures, the differences between the values of RAR, at which the charge sign reverses from negative to positive according to BSMP and TRAR, are more pronounced than these differences between the values of EW according to SKM and TAK. The reason is the different relative velocities, 3 m/s and 8 m/s at which the laboratory experiments were conducted, respectively in *Saunders et al.* (1991) and *Takahashi* (1978).

3. Numerical simulations and results

Simulations are performed to test the difference in cloud charge structure obtained with parameterizations of non-inductive charging that depends on the effective water content on one hand, and on the rime accretion rate on the other hand. For this purpose, laboratory results of *Takahashi* (1978) and of *Saunders et al.* (1991) are used to study if the inclusion of the effect of the relative velocity on the charge transfer (by means of the rime accretion rate) affects the charge structure in the same direction using the two main parameterization schemes of non-inductive charge, Takahashi's and SKM.

The model used for the simulations is the same as in *Brooks et al.* (1997) and *Tsenova* and *Mitzeva* (2009). During the simulations, the charge transfer Q (in fC) to a riming target per ice crystal separation event is calculated by

$$Q = B d^a V^b q, \tag{6}$$

where d is the crystal size (m), V is the relative velocity between graupel and ice crystals (m/s), and q (fC) is determined from empirically derived equations linking q with T and EW or RAR (for TAK/SKM and TRAR/BSMP parameterizations, respectively). The constants B, a and b are tabulated in *Saunders et al.* (1991). The values of a, b, B_S (for *Saunders et al.* (1991) charge values obtained with V=3 m/s and d=110 μm), and B_T (for *Takahashi* (1978) charge values obtained with V=8 m/s and d=100 μm) are shown in *Table 1*. To generalize, the following parameterizations for the non-inductive charging (*Fig. 2*) are tested:

(1) SKM: equations presented in *Saunders et al.* (1991) for the separated charge q_s, and

$$Q = B_S d^a V^b q_S(T, EW). \tag{7}$$

(2) BSMP: equations presented in *Brooks et al.*, (1997) for the separated charge q_s and

$$Q = B_S d^a V^b q_S(T, RAR). \tag{8}$$

(3) TAK: equations presented in *Tsenova* and *Mitzeva* (2009), for the separated charge q_T during Takahashi's experiment, and

$$Q = B_T d^a V^b q_T(T, EW). \tag{9}$$

(4) TRAR: equations presented here for the separated charge q_T during Takahashi's experiment, and

$$Q = B_T d^a V^b q_T(T, RAR). \tag{10}$$

In the model, convective clouds are composed of an active cloud mass representing the updraught region of convective clouds and a non-active cloud mass representing the environment surrounding the cloud updraught. The active cloud mass is modeled by successive spherical thermals ascending above cloud base, while the non-active cloud mass is modeled by previously risen thermals that have stopped at the level where their velocity is zero. The

model uses bulk microphysical parameterizations with five classes of water substances — water vapor, cloud water, rain, cloud ice, and precipitating ice (graupel). The cloud droplets are formed by condensation; raindrops are formed by autoconversion of the cloud droplets and grow by collision and coalescence with cloud drops (*Kessler*, 1969). Ice crystals originate from activation of ice nuclei in supercooled cloud droplets, their concentration is given by *Fletcher* (1962). Homogeneous freezing occurs below −40 °C. Graupel are formed by the freezing of rain drops (*Bigg*, 1953), contact nucleation of ice crystals and rain droplets (*Cotton*, 1972), and conversion of ice crystals (*Hsie et al.*, 1980). Ice crystals grow by deposition and riming. Graupel grows by deposition and coalescence with cloud and rain drops. Evaporation of rain drops and melting of graupel during their descent (*Farley* and *Orville*, 1986) as well as recycling is included. Cloud drops and ice crystals are assumed to be monodisperse and have negligible fall velocities, therefore, they move upward with the air. Particle size distributions for the precipitation species (rain drops and graupel) are parameterized using inverse exponential distributions of the general form. Precipitation fallout is calculated in the same manner as in *Cotton* (1972), and it comprises the portion of raindrops and graupel that have terminal velocities greater than the updraught speed.

Table 1. Values of the constants B_s (for *Saunders et al.* (1991) laboratory charge values), B_T (for *Takahashi* (1978) laboratory charge values), a and b

Charge sign	Crystal size (μm)	a	b	B_s	B_T
+Q	<155	3.76	2.5	4.9×10^{13}	6.1×10^{12}
+Q	155–452	1.9	2.5	4×10^{6}	5×10^{5}
+Q	>452	0.44	2.5	52.8	6.5
-Q	<253	2.54	2.8	5.24×10^{8}	4.3×10^{7}
-Q	>253	0.5	2.8	24	2

The recycling of precipitating particles is possible in the model through the incorporation of the mass of raindrops and graupel falling out from the upper ascending successive thermals. In the model, ice crystals and graupel in ascending thermals, together with larger falling graupel, are the electric charge carriers in the cloud model.

Two different cloud cases were simulated: C1 and C2. Some of their microphysical and dynamical properties can be seen in *Table 2*. From the table it is visible that the two simulated cases have similar maximum values of the water/ice species contents. However, the maximum updraft velocity in C2 is almost twice as large as the maximum updraft velocity in C1. The maximum mean terminal velocity of graupel particles in C2 is larger than that of C1

(9.5 m/s and 8.17 m/s, respectively) and it is achieved higher in the cloud (at 9.4 km above cloud base compared to 2.8 km above cloud base in C1).

Table 2. Microphysical and dynamical properties of the simulated cloud cases C1 and C2: CB – cloud base height (km), CWCmax – maximum cloud water content (g/m^3), CICmax – maximum cloud ice content (g/m^3), GCmax - maximum graupel content (g/m^3), Wmax – maximum updraft velocity (m/s), Vmax - maximum graupel mean fall velocity (m/s); the height and the model time of their achievement are indicated

	CB	CWCmax	CICmax	GCmax	Wmax	Vmax
C1	3.9 (~1°C)	1.3 11 min, 2.1 km	1.1 21.5 min, 5 km	0.2 18.5 min, 2.8 km	17.4 23.5 min, 6.9 km	8.17 18.5 min, 2.8 km
C2	2.9 (~11°C)	1.42 12 min, 3 km	0.9 12.5 min, 6.3 km	0.2 14.5 min, 3.4 km	29.74 18.5 min, 7.7 km	9.5 19 min, 9.4 km

Fig. 3 shows the total charge density, the density of the charge carried by ice crystals, and the density of the charge carried by graupel particles in one of the thermals (chosen in a way to represent the most active charging in the C1 cloud), which ascended between the 12th and 24th minutes of the model time (MT), obtained by the different parameterizations SKM, BSMP, TAK, and TRAR. The charge densities are presented as a function of cloud temperature. With the four parameterizations, the obtained charge distribution consists of a negative charge below and a positive one above. However, the temperature interval with negative total charge density is the smallest with the TRAR parameterization (at $T_a > -21$°C) and the largest with the BSMP parameterization (at $T_a > -31$°C). The largest negative total charge density is simulated with the SKM parameterization (~ −6 nC/m^3) . In the upper part of the thermal, the charge obtained with the four parameterizations is positive, reaching the highest positive charge density with the SKM parameterization – above 6 nC/m^3. Using parameterizations based on Takahashi's laboratory experiments (TAK and TRAR), the ice crystals are carriers of positive charge in this thermal, while the graupel particles carry negative charge, because the cloud conditions are similar to the conditions of negative charge in the *EW / T* and *RAR / T* diagrams in *Fig. 2*. Using parameterizations based on *Saunders et al.*, (1991) (SKM and BSMP), at higher temperatures the ice crystals are negatively charged, which is well pronounced when the BSMP parameterization is used (the crystal charge density is negative at $T_a > -30$ °C, where it reaches values above –1 nC/m^3), as in this region *RAR* is above 3.3 g/m^{2}s. In a very narrow temperature region, ice crystals are negatively charged with a weak negative charge density (~ 0.1 nC/m^3) when the SKM parameterization is used, due to the fact that *EW* is not high enough to maintain the positive charge of graupel in the *EW / T* diagram in *Fig. 2*.

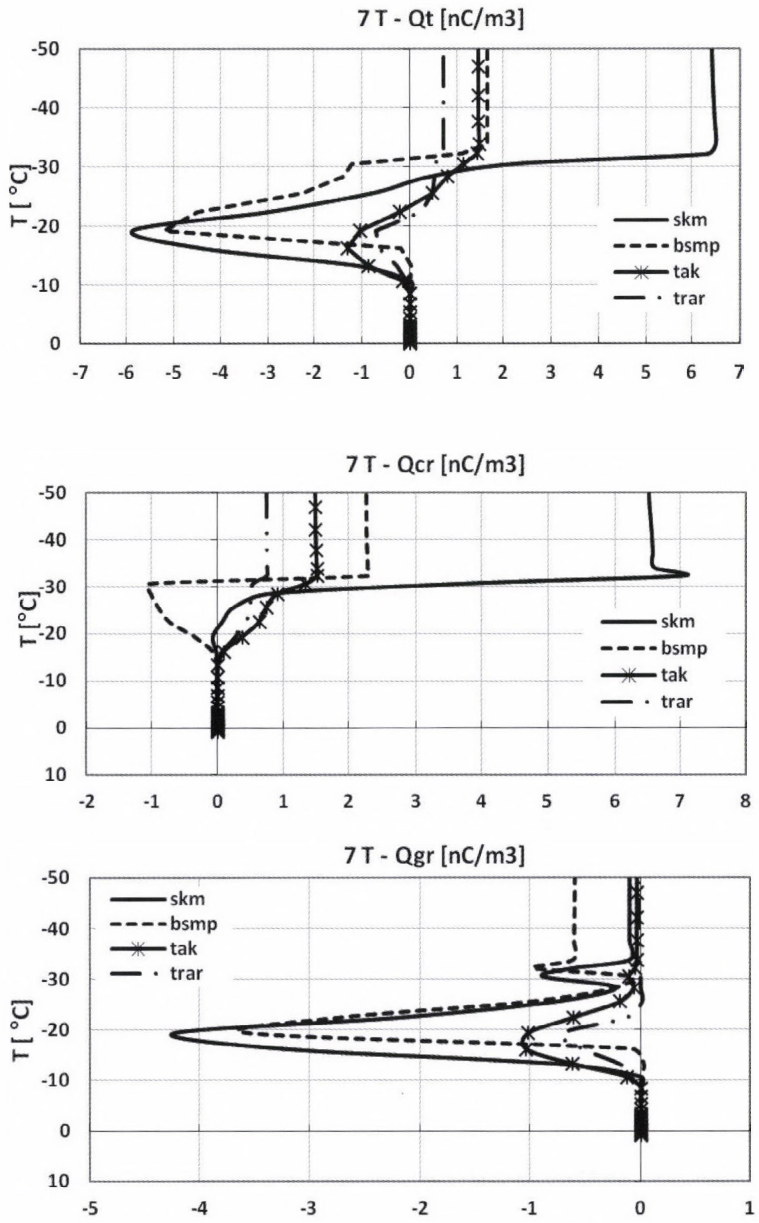

Fig. 3. C1 case: Total charge density (Qt), the density of the charge carried by the ice crystals (Qcr) and the density of the charge carried by graupel particles (Qgr) in the 7th thermal, which ascended between the 12th and 24th minutes of the model time obtained by the different parameterizations SKM, BSMP, TAK, and TRAR. The charge densities in nC/m^3 are presented as a function of the cloud temperature.

Fig. 4 shows the total charge density as a function of the height above the cloud base Z (km) and the model time MT (min) obtained with TAK, TRAR, SKM, and BSMP parameterizations. Using Takahashi based parameterizations (TAK and TRAR), the cloud charge structure consists of a normal dipole (a negatively charged region at the lower part of the cloud and a positively charged one above it) until 22 min MT. When TRAR (the *RAR* based parameterization) is used, a lower positively charged region appears, which leads to the formation of a normal tripolar structure. Using the results of Saunders, between 14 and 16 min MT an inverted tripolar structure forms – a positive charge between two negative ones below and above it. The cloud charge structure obtained with BSMP (*RAR* based parameterization) is an inverted tripole during almost the whole simulation. However, considering the maximum values of the total charge density obtained with the different parameterizations, as well the maximum values of the charge carried by ice crystals and graupel particles shown in *Table 3*, one can see that the maximum negative total charge density using all parameterizations is around –15 °C, while the maximum positive total charge density is at temperatures lower than –30 °C.

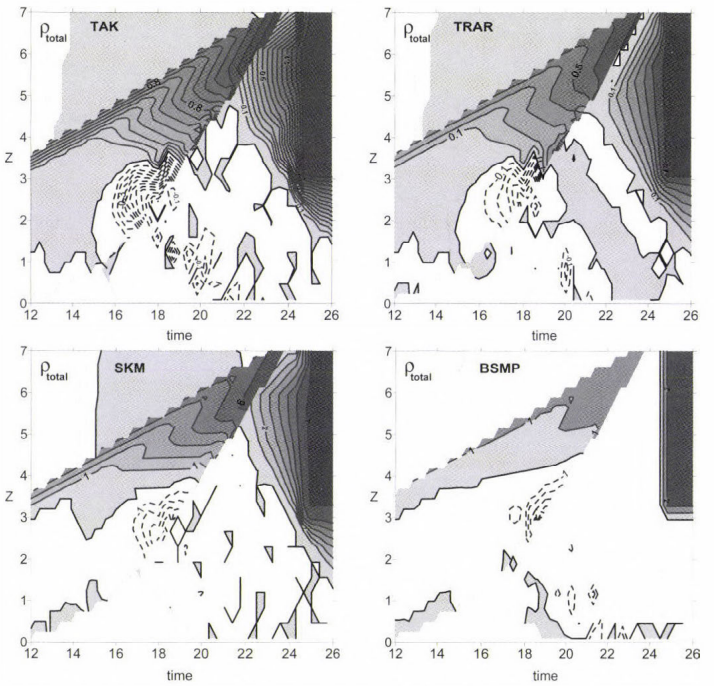

Fig. 4. C1 case: Total charge density as a function of Z (km) – height above the cloud base, and the model time (min) obtained with TAK, TRAR, SKM, and BSMP parameterizations (dark background with bold isolines indicates positive charge; bright background with dashed isolines indicates negative charge). Information on maximum values of positive and negative total charge densities, as well the height and the model time of their achievements can be seen in *Table 3*.

Table 3. C1 case: Maximum values of the negative (min) and positive (max) total charge density in nC/m^3, and of the charge density "carried" by ice crystals (Qcr) and graupel particles (Qgr) obtained with TAK, TRAR, SKM, and BSMP parameterizations

	TAK	**TRAR**	**SKM**	**BSMP**
Qt	–1.28/1.48	–0.7/0.7	–5.85/6.5	–5.2/2.2
min/max	18 min/21.5 min	18.5 min/ 24.5 min	18.5 min/21.5 min	18.5 min/24.5 min
	2.4 km/4.9 km	2.8 km/7.6 km	2.8 km/4.9 km	2.8 km/4.9 km
Qcr	~0/1.52	~0/0.7	~0/7.1	–1.04/2.28
min/max	12.5 min/21 min	11 min/21.5 min	18.5 min/21 min	20.5 min/21 min
	1.5 km/4.6 km	1.7 km/4.9 km	2.8 km/4.6 km	4.3 km/4.6 km
Qgr	–1.03/~0	–0.7/~0	–4.23/~0	–3.54/~0
min/max	18 min/13 min	18.5 min/19.5 min	18.5 min/16 min	18.5 min/17.5 min
	2.4 km/2.8 km	2.8 km/3.6 km	2.8 km/2.2 km	2.8 km/2.0 km

Fig. 5 shows the total charge density, the density of the charge carried by the ice crystals, and the density of the charge carried by graupel particles in one of the thermals in simulated C2 cloud obtained by the different parameterizations SKM, BSMP, TAK, and TRAR. The chosen thermal (as representing the most active charging in the cloud) ascended between 8 and 21 min MT. As mentioned above, the C2 cloud case has microphysical properties close to C1, at least regarding the maximum values of the water/ice species. However, the updraft velocity in C2 is almost twice as high as in C1. In C2, there are graupel particles in a wider region compared to C1, especially at lower temperatures, while in C1, there are no graupel above the level –40 °C. However, the total charge density in C2 is considerably lower than that of C1 using all parameterizations. The analysis of microphysical properties showed that the conditions in the larger part of C2 are close to those near the reversal lines in EW/T and RAR/T diagrams, thus, the charge density does not have the possibility to accumulate to higher values. This can be seen in *Fig. 5*. The total charge density alternates between positive and negative values when all parameterizations are used. It is the most "stable" when TAK is used. In this case Qt is negative at $T_a > -15$ °C, and positive above this level. When the TRAR parameterization is used, the total charge density is similar to the one obtained with TAK, but close to the cloud top $Qt < 0$ with TRAR. Similar, even more pronounced negative total charge at the cloud top is obtained with SKM and BSMP. This negative charge at high cloud level is carried by graupel that come from lower levels where they have been charged negatively during their interactions with ice crystals.

From *Fig. 6* it is visible that between 12 and 20 min MT using the TAK parameterization, the cloud is a normal dipole, while using TRAR, SKM, and BSMP gives an inverted tripole. This can be confirmed by *Table 4*, where the achievements of the maximum negative charge densities is later and higher in the cloud compared to the achievements of maximum positive charge densities

when TRAR, SKM, and BSMP parameterizations are used, which suggests inverted charge structures. After 20 min MT, the charge structure obtained with all parameterizations is a normal dipole.

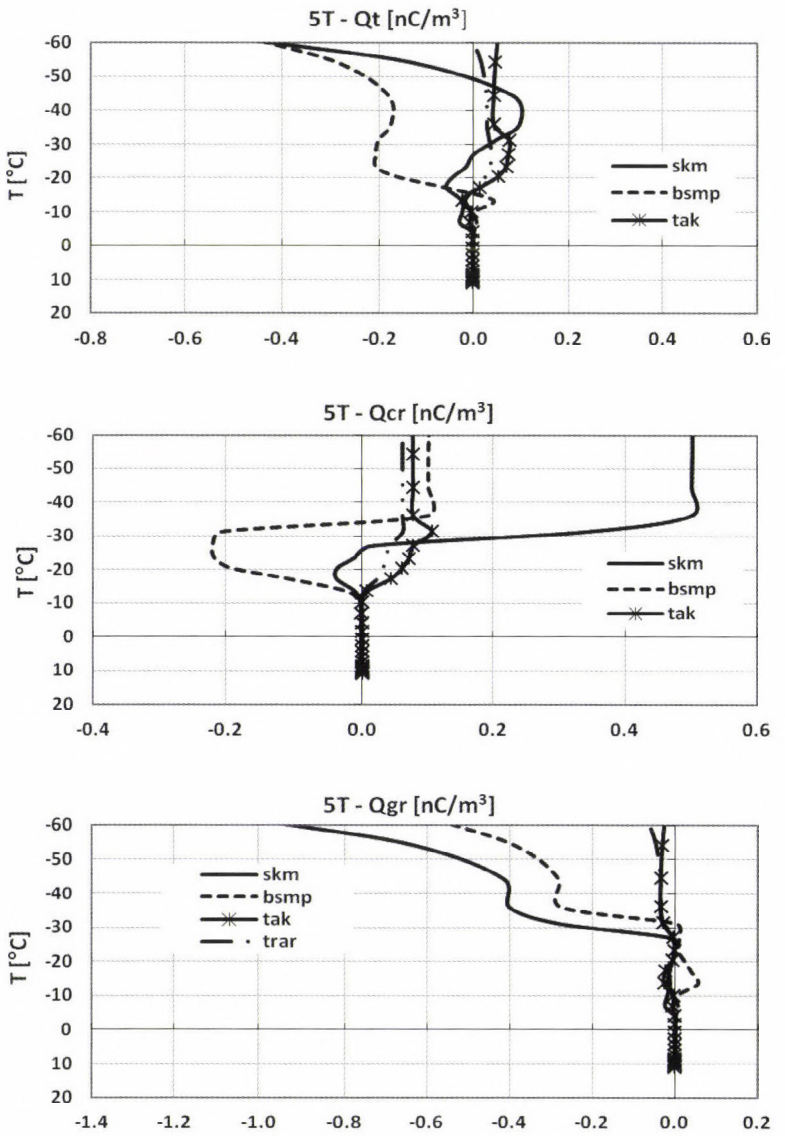

Fig. 5. C2 case: Total charge density (Qt), the density of the charge carried by the ice crystals (Qcr), and the density of the charge carried by graupel particles (Qgr) in the 5th thermal, which ascended between 8th and 21th minutes of the model time obtained by the different parameterizations SKM, BSMP, TAK, and TRAR. The charge densities in nC/m^3 are presented as a function of the cloud temperature.

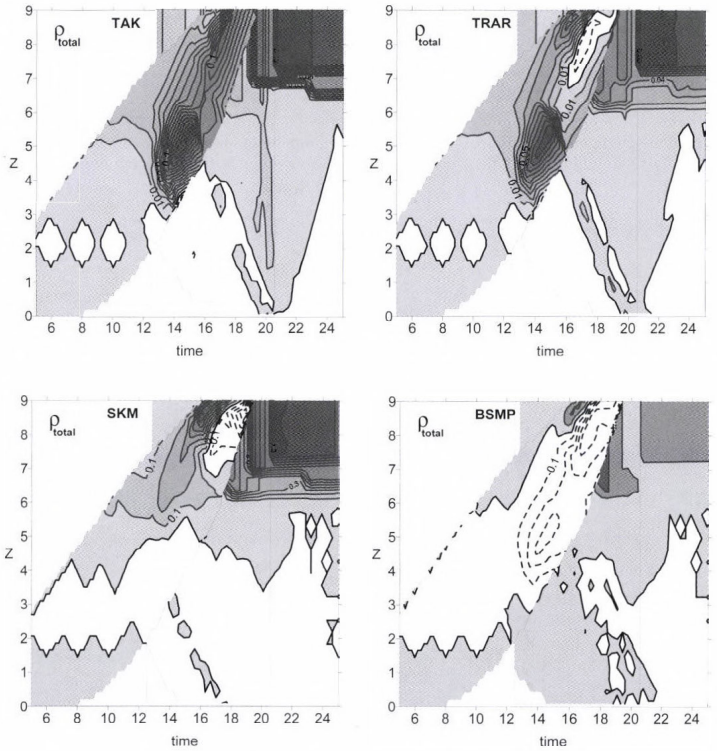

Fig. 6. C2 case: Total charge density as a function of *Z* [km] – height above the cloud base, and the model time obtained with TAK, TRAR, SKM, and BSMP parameterizations (dark background with bold isolines – positive charge; bright background with dashed isolines – negative charge). Information on maximum values of positive and negative total charge densities, as well the height and the model time of their achievements can be seen in *Table 4*.

Table 4. C2 case: Maximum values of the negative (min) and positive (max) total charge density in nC/ m^3, and of the charge density "carried by" ice crystals (Qcr) and graupel particles (Qgr) obtained with TAK, TRAR, SKM, and BSMP parameterizations

	TAK	**TRAR**	**SKM**	**BSMP**
Qt	–0.02/0.16	–0.02/0.1	–0.7/0.9	–0.6/0.3
min/max	14.5 min/15 min	17 min/ 15 min	19.5 min/16.5 min	19.5 min/17 min
	3.4 km/5.5 km	8 km/5.5 km	9.4 km/8.8 km	9.4 km/9.1 km
Qcr	–0.02/0.2	~0/0.4	–0.09/0.9	–0.4/0.3
min/max	13.5 min/15 min	14 min/15 min	13.5 min/13.5 min	15 min/13.5 min
	2.6 km/5.5 km	3 km/5.5 km	4.3 km/5.8 km	5.5 km/5.8 km
Qgr	–0.03/0.05	–0.07/~0	–1.2/0.1	–0.7/0.06
min/max	17.5 min/13.5 min	19.5 min/12 min	19.5 min/13.5 min	19.5 min/15 min
	6.1 km/5.8 km	9.4 km/3.0 km	9.4 km/7.2 km	9.4 km/5.5 km

4. Conclusions

In the present study a new parameterization of *Takahashi* (1978) laboratory data for non-inductive charging is proposed. This parameterization represents the separated charge as a function of the rime accretion rate, which takes into account the relative velocity between the interactive ice particles additionally to the effective water content and the temperature in the cloud. Numerical simulations using a 1.5-D model (suitable to simulate thundercloud core during growth stage) are performed for two different cloud cases, where the cloud electrification is parameterized based on the two sets of laboratory experiments *Takahashi* (1978) and *Saunders et al.* (1991), as the charge is calculated by means of the effective water content, as well as by means of the rime accretion rate. Results show that using parameterizations based on the data of *Saunders et al.* (1991) (SKM and BSMP), the total charge density is larger than the total charge density simulated with parameterizations based on the data of *Takahashi* (TAK and TRAR). Additionally, the different manner for representing the charge (as a function of the effective water content or the rime accretion rate) leads to more considerable differences in cloud charge structure when the parameterizations of *Saunders et al.* are used, comparing to the cases when parameterizations of Takahashi are used, due to different relative velocities during the two laboratory experiments.

As mentioned above, the present work is directed to give a better understanding of the effect of the scheme used for non-inductive charging on thundercloud electrification, without intending to make conclusions regarding which of the parameterizations are better suited to the realistic simulation of electrical charging in real clouds. Moreover, in Saunders et al. (2006) it was suggested that equations for their laboratory data should be used for simulations of the non-inductive charge transfer, when the interacting particles have had time to come to a steady growth state in their environment, while equations for laboratory data of Takashi may apply for simulations of charging in cloud regions where slow-growing ice crystals in a low-supersaturated environment are entrained into a region of high supersaturation. This case may be relevant to regions of clouds where entrainment has reduced the cloud supersaturation, and subsequent mixing of particles from regions with different saturation values will lead to transient growth that may influence the charge sign during crystal/graupel collisions. Thus, numerical simulations with a 3-D cloud model, where parameterization for non-inductive charging based on *Saunders et al.* (1991) (SKM or BSMP) is used for calculating the charging between interacting ice particles moving with the updraft, and parameterization for non-inductive charging based on the *Takahashi* (1978; TAK or TRAR) is used for calculating the charging between particles that interact at the regions between the updraft and downdraft are necessary for more adequate simulations of thunderstorm electrification.

References

Barthe, C., Pinty, J.P., 2007: Simulation of electrified storms with comparison of the charge structure and lightning efficiency. *J. Geophys. Res. 112*, D19204.

Bigg, E.K., 1953: The supercooling of water. *Proc. R. Soc., London, Ser. B 66*, 688–694.

Brooks, M., Saunders, C.P.R., Mitzeva, R.P., Peck, S.L., 1997: The effect on thunderstorm charging of the rate of rime accretion by graupel. *J. Atmos. Res. 43*, 277–295.

Cotton, W., 1972: Numerical simulation of precipitation development in super-cooled cumuli — part II. *Mon. Weather Rev. 100*, 764–784.

Farley, R.D., Orville, H.D., 1986: Numerical modelling of hailstones and hailstone growth. I.: preliminary model verification and sensitivity tests. *J. Appl. Meteorol. 25*, 2014–2036.

Fletcher, N.H., 1962: *The Physics of Rainclouds*. Camb. Univ. Press.

Helsdon, J.H., Wojcik, W.A., Farley, R.D., 2001: An examination of thunderstorm-charging mechanisms using a two dimensional storm electrification model. *J. Geophys. Res. 106*, 1165–1192.

Hsie, E., Farley, R.D., Orville, H., 1980: Numerical simulation of ice-phase convective cloud seeding. *J. Appl. Meteorol. 19*, 950–977.

Jayaratne, E.R., Saunders, C.P.R., Hallett, J., 1983: Laboratory studies of the charging of soft-hail during ice crystal interactions. *Q. J. Roy. Meteorol. Soc. 109*, 609–630.

Kessler, E., 1969: On the Distribution and Continuity of Water Substance in Atmospheric circulations. *Meteorol. Monogr. Boston, 10*, No 32.

Mansell, E.R., MacGorman, D.R., Ziegler, C.L., 2005: Charge structure and lightning sensitivity in simulated multicell thunderstorm. *J. Geophys. Res. 110*, D12101.

Mitzeva, R., Tsenova, B., Albrecht, R., Petersen, W., 2009: A study of charge structure sensitivity in simulated thunderstorms. *Atmos. Res. 91*, 299–309.

Pereyra, R.G., Avila, E.E., Castellano, N.E., Saunders, C.P.R., 2000: A laboratory study of graupel charging. *J. Geophys. Res. 105*, 20803–20812.

Saunders, C.P.R., Keith, W.D., Mitzeva, R.P., 1991: The effect of liquid water on thunderstorm charging. *J. Geophys. Res. 96*, 11007–11017.

Saunders, C.P.R., Bax-Norman, H., Avila, E. E. and Castellano, N. E., 2004: A laboratory study of the influence of ice crystal growth conditions on subsequent charge transfer in thunderstorm electrification. *Q. J. Roy. Meteorol. Soc., 130*, 1395-1406.

Saunders, C.P.R., Bax-Norman, H., Emersic, C., Avila, E.E., Castellano, N.E., 2006: Laboratory studies of the effect of cloud conditions on graupel/crystal charge transfer in thunderstorm electrification. *Q. J. Roy. Meteorol .Soc. 132*, 2655–2676.

Takahashi, T., 1978: Riming electrification as a charge generation mechanism in thunderstorms. *J. Atmos. Sci. 35*, 1536–1548.

Takahashi, T., and *Miyawaki, K*, 2002: Reexamination of riming electrification in a wind tunnel. *J. Atmos. Sci. 59*, 1018–1024.

Tsenova, B.D., Mitzeva, R.P., 2009: New parameterization of non-inductive charge transfer based on previous laboratory experiments. *Atmos. Res. 91*, 79–86.

IDŐJÁRÁS

Quarterly Journal of the Hungarian Meteorological Service
Vol. 115, No. 4, October–December 2011, pp. 265–273

Tropospheric scintillation measurements in Ku-band satellite signals on Earth-space paths with low elevation angle

Jit Singh Mandeep[1,2 *], **Anthony Cheng Chen Yee**[1], **Mardina Abdullah**[1,2], and **Mohammad Tariqul Islam**[2]

[1]*Department of Electrical, Electronic & Systems Engineering, Faculty of Engineering & Built Environment, University Kebangsaan Malaysia, 43600 UKM, Bangi, Selangor Darul Ehsan, Malaysia*

[2]*Institute of Space Science, Faculty of Engineering & Built Environment, University Kebangsaan Malaysia, 43600 UKM, Bangi, Selangor Darul Ehsan, Malaysia*
E-mail; mardina@eng.ukm.my, tariqul@ukm.my

[*]*Corresponding author E-mail; mandeep@eng.ukm.my*

(Manuscript received in final form April 26, 2011)

Abstract—This paper discusses the tropospheric scintillation of a KU-band satellite antenna, which installed at the University Sains Malaysia (USM), Malaysia, on an elevation angle of 40.1 °, at frequency of 12.255 GHz. Tropospheric scintillation in this context means rapid fluctuation of radiowave signals occuring during data transmission due to the turbulence at the atmosphere when the signal propagates. It occurs every day and tends to affect the quality of the communication link, especially for the link that utilizes frequency band higher than 10 GHz. The paper compares the measured tropospheric scintillation data with gamma and normal (Gaussian) distributions for short-term and long-term scintillation distributions. The findings show that for short-term scintillations, the probability density function (PDF) will tend to follow gamma distribution and for long-term scintillation, the PDF will follow normal distribution. The results are very useful to develop a new tropospheric scintillation model for Malaysia and for other areas with similar climate.

Key-words: tropospheric scintillation, satellite communication, Ku-band satellite signals, probability density function

1. Introduction

Tropospheric scintillation can be defined as rapid fluctuation of the amplitude or phase of a radiowave caused by changes of refractive index at the altitude. It is caused by the humidity and temperature of the atmosphere. The effects of tropospheric scintillation are seasonal and vary from day to day with the local climate (*Mandeep* and *Yun Yang Ng*, 2010). The scintillations effect is needed to take into the link budget design of millimeter-wave communication system, as it will bring huge impact to the quality of the signal. For low-margin systems operating at high frequency (Ku-band and above) and low elevation angle (*Mandeep* and *Yun Yang Ng*, 2010), signal degradation caused by scintillation can be more dominant compared to rain attenuation (*Mandeep et al.*, 2010). For this reason, accurate scintillation models are needed to achieve satisfactory signal quality for daily satellite communication usage.

To predict the signal fade and enhancement, there is a need to determine the short-term (several minutes) and long-term scintillation pattern (4 months) throughout the year. Short-term and long-term fluctuations are to be calculated based on the collected data. Objective of this paper is to verify the mathematic model that fits to the short-term and long-term scintillation patterns in Malaysia. Probability density functions (PDF) of short-term (several minutes) and long-term 4 months scintillations will be compared with gamma and normal distributions to verify which distribution fits to the tropospheric scintillation in Malaysia.

2. Methodology

For this data analysis, we obtain the signal parameter from a 12.255 GHz Superbird C beacon at elevation angle of 40.1 using a sampling rate of 1 minute. The beacon is located at the USM campus at Parit Buntar, Malaysia (5.170°N, 100.4°E). The data for this analysis is taken from January 1, 2009 to December 31, 2009. Apart from the satellite signal, weather informations such as humidity, temperature, air pressure, rain rate etc. are taken down using the same sampling rate for further analysis purpose. *Table 1* shows the ground station configuration for the Superbird C beacon.

Table 1. Satellite specification

Ground station location	5.170N, 100.40E
Beacon frequency	12.255 GHz
Elevation angle	40.10
Polarisation	Horizontal
Antenna configuration	Offset parabolic
Antenna Diameter	2.4 m
Satellite position	1440 E
Antenna height	57 m above sea level

The term "scintillation" means fast fluctuations of signal amplitude and phase, caused by atmospheric turbulence. This effect is due to turbulent irregularities in temperature, humidity, and pressure, which translate into small-scale variations in refractive index. An electromagnetic wave passing through this medium will then encounter various refraction and scattering effects, which will result in a multipath effect.

It is known that over relatively short time periods, where the meteorological conditions are fairly constant, scintillation amplitudes, in dB, follow a Gaussian distribution around the mean signal level which is zero. This is why they can be characterized by standard deviation σ, which is commonly referred to as scintillation intensity. For long time periods, the distribution of scintillation amplitude deviates significantly from a Gaussian probability density function (pdf, especially in the tails) (*Kassianides* and *Otung*, 2003).

Scintillation is defined in terms of the received log-amplitude signal, χ (in dB) that is related to the signal amplitude, A, the mean signal amplitude, $\langle A \rangle$, and the (zero-mean) fluctuating signal component $\Delta A = A - \langle A \rangle$, by

$$\chi = 20 log_{10}\left(1 + \frac{\Delta A}{A}\right). \tag{1}$$

Scintillation occurs continually in both rainy and clear sky conditions (*Mandeep*, 2009). Precaution is needed to take when rain occurs, since the amplitude-level of signal fluctuation is accompanied by the rain attenuation and needed to be removed to avoid inconsistency in data analysis. The measured data is inspected for any inconsistencies. The procedure to extract reliable scintillation statistics comprises both manual and automatic steps. Rain periods have been removed using rain gauge data. Visual inspection is performed in all data sequences to eliminate spurious and invalid data. All the valid measurements have been passed through a high-pass filter with a cutoff frequency (f_c) of 0.025 Hz, which allows isolating the fast variations caused by scintillation from other slowly varying signal components (*Otung et al.*, 1998). To examine the effect on scintillation statistics of the cutoff frequency, used for data filtering, 14 different values of (f_c) between 2 and 500 mHz were used. For each scintillation data set (obtained using a particular value of f_c), a goodness-of-fit test were performed to determine whether the 1 minute distribution of the scintillation amplitude followed a Gaussian pdf. The value of f_c must be carefully set. If f_c is too low, then non-scintillation effects are inadvertently included in the signal fades and enhancements about the mean level. On the other hand, if f_c is too high, then legitimate contributions to scintillation at Fourier components lower than the set value of f_c are excluded. Scintillation variance, that represents the best way to characterize scintillation intensity, has

been calculated as the square of the standard deviation of the signal amplitude (dB) over periods of 1 minute (*Otung et al.*, 1998).

The gamma distribution is a two-parameter continuous probability distribution. It has a scale parameter θ and a shape parameter k, where the mean and the variance are $k\theta$ and the $k\theta^2$. The probability density function of random variable, x, which is gamma-distributed with θ and k, can be formulated as (*ITU-R P. 618-10*, 2009):

$$x^{k-1}\frac{exp(-x/\theta)}{\Gamma(k)\theta^k}, \tag{2}$$

The normal distribution or Gaussian distribution is a continuous probability distribution that variates with mean, μ and variance, σ^2, that can be obtain using conventional statistic formula. The probability density function of the variable x that followes normal distribution is (*Marzano* and *d'Auria*, 1998)

$$f(x)=\frac{1}{\sqrt{2\pi\sigma^2}}e^{\frac{(x-\mu)^2}{2\sigma^2}}. \tag{3}$$

3. *Results and discussion*

Malaysia has an equatorial climate, producing a warm and wet weather due to its proximity to the equator. The temperature is maintained at around 25 – 28 °C, and the humidity is high all over the year with values between 72.2 and 82.3%. There are two monsoon winds that influence the rainfall in the different intervals of the year in Malaysia. The southwest monsoon usually occurs between May and September, bringing rainfall to the western side of Malaysia. On the other hand, the northeast monsoon starts from November and lasts till March, brining heavy rainfall to areas on the east side of Peninsular Malaysia (*Mandeep*, 2009). Since these two monsoons will increase the rain rate in Malaysia, it tends to have affect on the tropospheric scintillation probability distribution. *Table 2* shows the averaged temperature and humidity for each month in 2009.

A suggestion of the departure of the probability density function of a random variable from symmetry about the mean is given by its skewness $S=\mu_3/(\mu_1)^3$, where μ_1 is the first moment about the mean (or standard deviation) and μ_3 is the third moment about the mean. *Table 3* shows the values of standard deviation and skewness calculated for each month of 2009. All measured results report a negative skewness of scintillation amplitude distribution.

Table 2. Monthly temperature and humidity for year 2009

Month	Temperature (°C)	Humidity (%)
Jan	25.32	75.29
Feb	26.07	77.89
Mar	25.95	80.21
Apr	26.47	79.94
May	26.92	78.30
Jun	27.94	72.21
Jul	27.14	74.45
Aug	25.77	82.08
Sep	26.09	79.76
Oct	26.39	79.43
Nov	25.60	82.37
Dec	25.00	82.22

Table 3. Standard deviation and skewness of the probability density function for 2009

Month	Standard deviation (dB)	Skewness
Jan	0.20	−0.023
Feb	0.23	−0.060
Mar	0.09	−0.009
Apr	0.10	−0.020
May	0.15	−0.070
Jun	0.12	−0.015
Jul	0.11	−0.034
Aug	0.14	−0.040
Sep	0.18	−0.070
Oct	0.20	−0.005
Nov	0.14	−0.027
Dec	0.21	−0.120

The scintillation standard deviation shows some variations on a long-term basis (i.e., from several weeks), which are not Gaussian-distributed. This can be expressed as

$$p(\sigma)=\frac{1}{\sigma_1 \sigma ln10\sqrt{2\pi}} e^{-\frac{(log\,\sigma-m_1)^2}{2\sigma_1^2}}, \tag{4}$$

where m_1 is the mean value of $log\ \sigma$,
σ_1 is the standard deviation of $log\ \sigma$.

3.1 Short term scintillation analysis

In this paper, short term scintillation is taken as scintillation that occurs in an interval of 20 minutes in a day and accumulated into a month. With a sampling rate of 1 minute, for each set of data, scintillation data are processed and the PDF are plotted into graphs. The graph is then compared with the respective gamma and normal distributions.

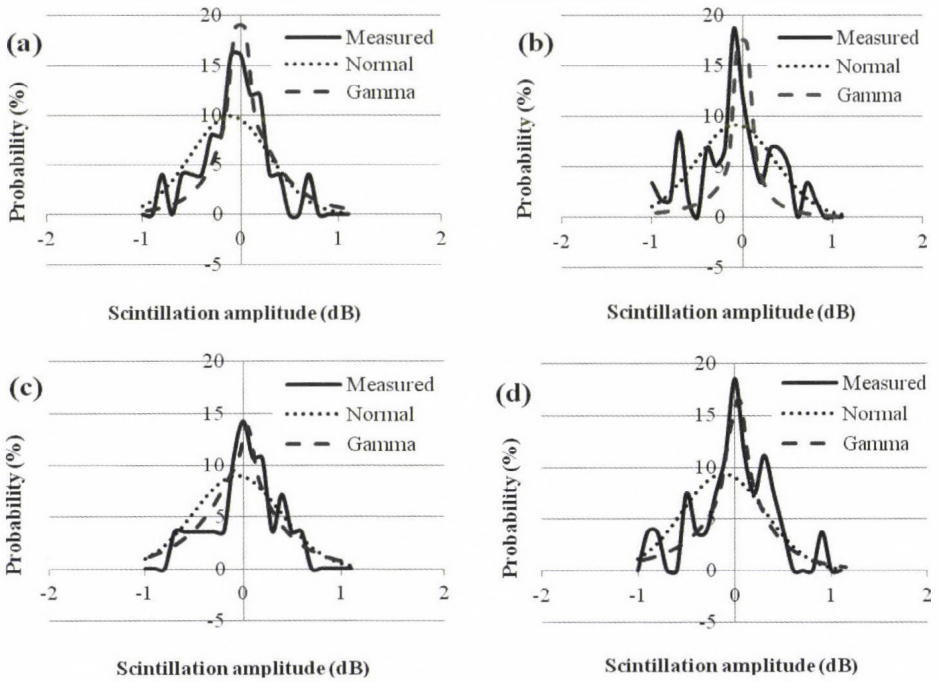

Fig. 1. Short-term scintillation for (a) January, (b) May, (c) September, and (d) December 2009.

Figs. 1(a) – (d) shows the short-term scintillation for every quarter of the year 2009. Each of the graphs represents a set of amplitude scintillation data in an interval of 20 minutes for each day and accumulated over a month. Due to the low sampling rate, the measured PDF for short-term scintillation looks a bit spiky. Regardless from the spiky graphs, the short-term scintillation data are similar to the gamma distribution function. Throughout the whole year, short-term scintillation is following gamma distribution without being affected by the monsoon season. The measured data have sharper edge on steeper curve and the 0 dB. These characteristics are similar to gamma distribution. Normal distribution is not suitable to predict short-term scintillation as the curves tend to be wider.

3.2 Long-term scintillation analysis

For long-term scintillation, the scintillation data is processed on a quarterly basis. In each quarter of the year, tropospheric scintillation data for every month will be averaged, and the PDFs are plotted into a graph. The graphs will be then compared to normal and gamma distributions for that particular time interval.

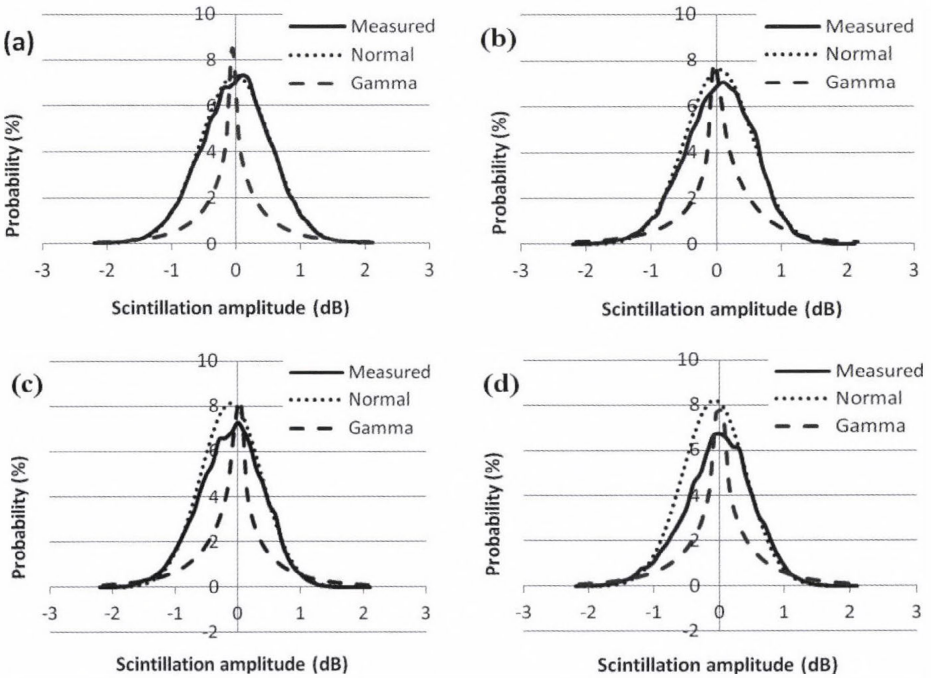

Fig. 2. Long-term scintillation for the (a) first quarter of 2009 (January 1 – March 31), (b) second quarter of 2009 (April 1 – June 30), (c) third quarter of 2009 (July 1 – September 30), and (d) fourth quarter of 2009 (October 1 – December 31).

Scintillation data for monthly period is mentioned as it will be averaged. Scintillation intensity is stationary on a time-scale of up to one month. The monthly tropospheric scintillation data were calculated based on

$$p(x)=\int_0^\infty p(\sigma_x)p(x/\sigma_x)d\sigma_x, \tag{5}$$

where σ_x is the standard deviation, σ_x^2 is the variance of the signal level, and

$$p(x/\sigma_x)=\frac{1}{\sigma_x\sqrt{2\pi}}exp\left[-\left(\frac{x^2}{2o_x^2}\right)\right]. \tag{6}$$

Figs. 2 (*a*) –(*d*) show scintillation data on quarterly basis for 2009. As it is shown in the graphs, for long-term scintillations, the distribution fits more to the normal distribution than gamma distribution. The measured scintillation PDF gives a bell-curve shape that identical to normal distribution. Gamma distribution has sharper edge at 0dB and it differs from the measured data; therefore, it is not likely to be used to predict long-term tropospheric scintillation. Overall, the measured data fit exceptionally close to the normal distribution, especially in the first two quarters of the year.

From *Table 2* we can observe, that there are increases in humidity from August to December. The last two quarters of the year vary more to normal distribution, and it may be caused by the increases of humidity due to the monsoon season.

Fig. 3 shows the tropospheric scintillation probability density function of year 2010. From the graph we can see, that throughout the year, the scintillation pattern follows the normal distribution. The measured scintillation amplitude has wider bell shape as in normal distribution and differs from gamma distribution in term of the curve shape.

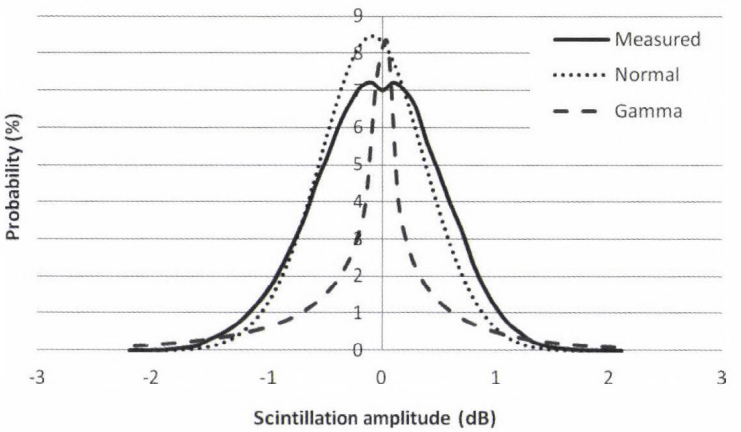

Fig. 3. Probability density function of measured data compared with normal and Gaussian distributions for 2010.

4. Conclusion

From the graphs presented in this paper, we can see, that short-term scintillation follows the gamma distribution closely while, on the other hand, long-term distribution follows the normal distribution. It is essential to verify the pattern of tropospheric scintillations in Malaysia before developing a new tropospheric scintillation model. For short-term scintillations, gamma distribution gives a more similar curve where the edge is sharper at the 0 dB level, so it is suitable to

predict the short-term scintillations. For long-term scintillations, normal distribution fits better to the scintillation pattern compared to the gamma distribution. Long-term scintillation has wider curve at both ends and less sharp edge at 0dB level, which is similar to the normal distribution.

Acknowledgements—The authors would like to acknowledge the University Kebangsaan Malaysia, University Sains Malaysia, MOSTI grant Science Fund (01-01-92-SF0670), UKM-GGPM-ICT-108-2010, UKM-DLP-2011-003 and the Association of Radio Industry Business (ARIB) of Japan for providing the instruments used for collecting the data.

References

ITU-R P. 618-10, 2009: *Propagation Data and Prediction Methods Required for the Design of Earth-Space Telecommunication systems*.ITU Radiocomm. Bureau, Geneva, 6 pp.

Kassianides, C.N. and *Otung, I.E.* 2003: Dynamic model of tropospheric scintillation on earth-space paths. *IEE Proc.-Microw Antenna Propg., 150*, 97–104.

Mandeep, J.S., 2009: Rain attenuation statistics over a terrestrial link at 32.6 GHz at Malaysia. *IET Micro., Anten. & Prop. 3*, 1086–1093.

Mandeep, J.S., 2009: Slant path rain attenuation comparison of prediction models for satellite applications in Malaysia. *J. Geophys. Res.-Atmos. 114*, D17108. doi:10.1029/2009JD011852.

Mandeep, J.S., and *Yun Yang Ng,* 2010: Satellite beacon experiment for studying atmospheric dynamics. *J. Inf. Millim. Tera. Wav. 31*, 988–994.

Mandeep, J.S., Ng, Y.Y., Abdullah, H., and *Abdullah, M.*, 2010: The study of rain specific attenuation for the prediction of satellite propagation in Malaysia. *J. Inf. Millim. Tera. Wav. 3*, 681-689.

Marzano, F.S. and *d'Auria, G.*, 1998: Model-based prediction of amplitude scintillation variance due to clear-air tropospheric turbulence on Earth-satellite microwave links. *IEEE Trans. Antennas Propag. 46*, 1506–1518.

Otung, I.E., Al-Nuaimi, M.O., Evans, B.G., 1998: Extracting scintillations from satellite beacon propagation data. *IEEE Trans. Antennas Propag. 46,* 1580–1581.

IDŐJÁRÁS

Quarterly Journal of the Hungarian Meteorological Service
Vol. 115, No. 4, October–December 2011, pp. 275–288

Estimation of structural icing intensity and geometry of aircrafts during different conditions – a fixed-wing approach

Zsolt Bottyán

Aviation Weather Laboratory, Department of Air Traffic Controller and Pilots' Training, Zrínyi Miklós National Defence University, P.O. Box 1, H-5008 Szolnok, Hungary
E-mail: bottyan.zsolt@zmne.hu

(Manuscript received in final form May 8, 2011)

Abstract—The estimation of aircraft structural icing characteristics is a very important procedure as the accreted ice layer may cause some dangerous effects for aircraft such as lift force degradation, increasing of drag force, and malfunction of control surfaces and sensors. The intensity and geometry of ice contamination on the surface of an aircraft depend on meteorological (cloud droplet size distribution, liquid water content, ambient temperature), aerodynamical (airspeed), and geometrical (size and shape of the aircraft) conditions, too. In this paper a 2D similar ice accumulation model is shown which is based on a cylindrical approximation of airfoil and the thermodynamics of icing processes. Applying this model, the intensity and geometry of accreted ice layer can be accessed on the wing of a popular fixed-wing aircraft Cessna-185 Skywagon in a special cold-pool-like weather situation. On the basis of our calculation it is clear, that the severity of icing phenomena strongly depends not only on the meteorological but also on aerodynamical conditions. On the other hand, this method can be adapted for an operational structural airframe icing severity forecasting.

Key-words: aviation meteorology, aircraft structural icing, icing severity, liquid water content, Cessna-185 Skywagon

1. Introduction

The airframe (structural) icing occurs when an aircraft flies mainly under IFR (instrument flight rules) condition (generally in cloud), the ambient static temperature is below zero, and supercooled water droplets impinge and freeze on the aircraft's unprotected surface. The ice accretions cause many dangerous problems during the flight such as reduced lift and increased drag forces,

significantly decreased angle of attack, strong vibrations and structural imbalances of aircrafts, malfunction of control surfaces and air pressure sensors, reduced visibility, and improper radio communication (*Bragg et al.*, 2005). On the other hand, there are some differences between the structural icing of fixed-wing aircrafts and rotorcrafts (helicopters), e.g., the different icing problem of helicopters along their rotor blades (*Gent et al.*, 1987; *Gent et al.*, 2000). On the basis of these facts, a reliable estimation of expected ice accretion during the proposed flight is very useful and important information for the pilots (*Jeck*, 1998; *Fuchs* and *Lütkebohmert*, 2001; *Lankford*, 2001; *Fuchs*, 2003).

Forecasting of airframe (structural) icing of aircrafts is a very complex procedure since the magnitude of the ice accretion on the aircrafts' surfaces highly depends on ambient meteorological and aerodynamical conditions and on aircraft's geometry, too. The rate and amount of structural ice accretion curiously depend on the followings (*Gent et al.*, 2000; *Lankford*, 2001; *Bragg et al.*, 2005):

- static ambient temperature of airflow around the aircraft,
- static air pressure at the level of flight,
- liquid water content (*LWC*) of cloud,
- cloud droplet size distribution,
- true airspeed (*TAS*) of aircraft, and
- shape and size of aircraft structures with the special regard to wings.

It is clear that the surfaces with high rate of ice accretion are located near the leading edge of wings and tail. They are relatively narrow and their positions are usually opposite the freestream. For that very reason, the ice accretion models have to approach the wing geometry well. In many 2D ice accumulation models a suitable cylinder is applied to describe the ice accretion characteristics along its surface because the cloud droplet trajectory calculation in the airflow around the cylinder is a relatively simple procedure (*List*, 1977; *Lozowski et al.*, 1983a; *Makkonen*, 1981; *Launiainen* and *Lyyra*, 1986; *Finstad et al.*, 1988; *Makkonen* and *Stallabrass*, 1987; *Mazin et al.*, 2001).

In our work we apply a 2D ice accretion non-rotating cylinder model based on the methods of *Lozowski et al.* (1983a) estimating the rate and geometrical characteristics of ice contamination on a small popular aircraft such as Cessna-185 Skywagon under different aerodynamic and meteorological conditions.

2. The ice accretion model

The applied ice accretion model is based on the quasi-stationary heat balance equation for a freezing surface which is assumed to define the thermodynamics of icing phenomena, first described by *Ludlam* (1951) and *Messinger* (1953). The local collection efficiency calculation used by *Langmuir* and *Blodgett*

(1946), *Lozowski et al.* (1983a), *Finstad et al.* (1988) and the ice growth estimation along the cylinder surface is described by *Lozowski et al.* (1983a).

Assume a non-rotating horizontal cylinder with a diameter of D_c located in a uniform airstream with the velocity of U (freestream velocity). The streaming air under cloudy circumstances contains supercooled droplets with the concentration of W. Supposing that the airstream and droplets are in thermodynamic and mechanical equilibrium, the temperature of airstream T_a equals the droplet temperature. Apparently, the velocity of supercooled droplets far from the cylinder is also U.

In order to calculate the local impingement of water droplets, we divided the upwind surface of the cylinder into angular sectors of 5° and centered the angles $\theta_i = 5i°$, $i = 1,2,\ldots,18$. The applied droplet size characteristics are also discretized by establishing 9 diameter categories with 5 μm wide intervals centered the diameters $D_j = 5j$ μm, $j = 1,2,\ldots,9$. We assume that the droplets have the same size (central diameter) in each category. On the basis of assumptions mentioned above the local droplet collision efficiency can be calculated for all angular sectors and droplet size categories as follows:

$$\beta_i = \sum_j f_j \beta_{ij}, \tag{1}$$

where f_j is the fraction of total water mass flux in the airflow, containing droplets in the jth diameter category. After that, the liquid water mass flux impinging all sectors along the upstream face of the cylinder can be expressed as:

$$R_{wi} = \beta_i UW. \tag{2}$$

The quasi-stationary heat balance equation for a freezing surface is given by

$$Q_c + Q_e + Q_v + Q_k + Q_f + Q_w + Q_i + Q_r + Q_w^* + Q_f^* = 0, \tag{3}$$

where

- Q_c is the sensible heat flux between freezing surface and airstream;
- Q_e is the latent heat flux of evaporation;
- Q_v is the viscous aerodynamic heating due to airstream;
- Q_k is the flux of kinetic energy of impinged droplets on the icing surface;
- Q_f is the latent heat flux of accretion due to freezing of impinging water;
- Q_w is the sensible heat flux required to warm the freezing water droplets;
- Q_i is the heat flux between the iced and the underlying surface;

– Q_r is the long-wave radiative heat flux;

– Q_w^* is the sensible heat flux required to heat the runback and shedding part of impinging water (similar to Q_w);

– Q_f^* is like Q_f but for runback water only.

If the physical and aerodynamic conditions allow the existence of any unfrozen water on the icing surface (wet-growth ice accretion), the mass of it in any angular sectors is supposed to be moved to the next downstream sector by airstream. On the other hand, we also assume the runback water will be shed into the airstream at $\theta = 90°$. The items in Eq. (3) are formularized as follows:

$$Q_c = h(T_a - T_s), \tag{4}$$

where h is the heat transfer coefficient, T_a and T_s are the temperatures of airstream and icing surface, respectively. The calculation of h is based on the results of *Achenbach* (1977), and we applied the rough cylinder case (because the icing process produces a rough cylinder surface).

The evaporation heat flux term is given by

$$Q_e = h\left(\frac{Pr}{Sc}\right)^{0.63} \frac{\varepsilon l_v}{pc_p}(e_a - e_s), \tag{5}$$

where Pr and Sc are the Prandtl and Schmidt numbers, ε is the ratio of the molecular weights of water vapor and dry air, p is the static pressure of air in the freestream, c_p is the specific heat capacity of dry air at a constant pressure, l_v is the latent heat of vaporization, and finally, e_a and e_s are the saturation water vapor pressures of moist air at T_a and T_s. If the accretion is dry, the latent heat of sublimation l_s has to be applied.

The viscous heating can be given by

$$Q_v = \frac{hr_c U^2}{2c_p}, \tag{6}$$

where r_c is the local recovery factor along the cylinder surface described by *Seban* (1960). This term explains the adiabatic heating due to the air compressibility at higher velocities and the frictional heating in the boundary layer. This factor is very important when the Mach number of airstream is higher than 0.3 (in this case the compressibility of air will be higher than 5%).

The kinetic energy flux of droplets can be calculated by

$$Q_k = \frac{1}{2} R_w U^2, \tag{7}$$

where R_w is the droplet mass flux and $R_w = \beta WU$.

During the freezing of impinging supercooled water the latent heat flux is

$$Q_f = nR_w l_{fs}, \tag{8}$$

where l_{fs} is the latent heat of freezing at T_s and n is the fraction of accreted mass of impinging water. It is obvious, that if $T_s < 273.15$ K then $n = 1$ (dry-growth icing) and in the case of $T_s = 273.15$ K, $n < 1$ (wet-growth icing and there are some runback water along the icy surface of the cylinder).

The sensible heat flux is required to warm the impinging droplets to the equilibrium temperature T_s, and it is given by

$$Q_w = R_w \bar{c}_w (T_a - T_s), \tag{9}$$

where $\bar{c}_w$ is the average specific heat of water between T_a and T_s. Its value is a constant in this model.

The linear approximation of radiative heat flux between the droplets and accreted surface can be written by

$$Q_r = \sigma\left(\varepsilon_a T_a^4 - \varepsilon_s T_s^4\right) = a(T_a - T_s), \tag{10}$$

where ε_a and ε_s are the radiative emissivity of air and surface, respectively, σ is the Stefan-Boltzmann constant, and a is a coefficient.

The amount of existing runback water (unfrozen part of impinged droplets in a given sector) also plays an important role in the heat exchange between the sectors. We suppose, that there are not any parallel flows to the cylinder axis, and the leaving part of runback water (with the steady-state temperature of the given sector) influences the next sector's heat balance only. Obviously the amount of entering runback water adjusts the steady-state temperature in the given sector thus the heat flux in connection with it is described by

$$Q_w^* = R_w^* \bar{c}_w \left(T_s^* - T_s\right), \tag{11}$$

where R_w^* is the mass flux of runback water entering the given sector, T_s^* is the

temperature of runback water. It is obvious the T_s^* equals 0 °C if there are any runback water (because the steady-state condition). Evidently there is not any runback water into the first sector and the entering part of runback water from the first sector to the second one is the half of the amount of total outflow runback water from the first sector (it is based on the cylinder geometry). The latent heat flux of freezing the runback water is given by

$$Q_f^* = nR_w^* l_{fs} . \tag{12}$$

In our model the Q_i heat flux was omitted and taken into account by Eqs. (4)–(12). In this case, Eq. (3) is a non-linear differential equation which can be solved by numerically within each sector. The two unknowns in Eq. (3) are T_s and n. The solving procedure of Eq. (3) is described by *Gent et al.* (2000) and *Saeed* (2000).

After the calculation of impinging water flux (R_{wi}), runback water flux (R_{wi}^*), and freezing faction (n_i), we can determine the icing flux (R_i) in all sectors:

$$R_i = n_i (R_{wi} + R_{wi}^*) . \tag{13}$$

The calculation of the ice growth is given by

$$h_i = \frac{2R_i \delta t / \rho_i}{1 + \left(1 + \frac{4R_i \delta t}{\rho_i D_c} \right)^{0.5}} , \tag{14}$$

where h_i means the local thickness of accretion, δt is the accretion time, and ρ_i is the ice density (*Lozowski et al.*, 1983a). The application of this ice growing approach is limited in time because we have to assume that the ice accretion phenomena does not significantly influence the environment of airstream and the heat exchange around the surface. However, this approach can be applied to estimate the ice accretion rate if we use a short time interval (δt). Experimental results of wind tunnels have confirmed the applicability of Eq. (14) if the time interval is not longer than 5–7 minutes (*Lozowski et al.*, 1983b). On the other hand, the shapes of accreted ice contamination grew during the wind tunnel experiments are very similar to those calculated by the applied ice growth model. These experiments were executed under conditions such as (–5 °C)–(–15 °C) temperature, 30.5–122 m s^{-1} airspeed, 0.13–1.27 g m^{-3} *LWC*, and 1–10 minutes time intervals, respectively (*Lozowski et al.*, 1983b).

3. Methods

The ice accretion model described in Section 2 can be used to estimate the amount, rate and, geometry of ice contamination not only along a given cylinder but also along a surface that has the similar curvature (for example, a fixed-wing aircraft airfoil). For the real icing calculation, we applied the twice leading edge radius of the airfoil as cylinder diameter (*Tsao* and *Anderson*, 2005). Our examined fixed-wing aircraft was the popular Cessna-185 Skywagon (*Fig. 1*).

Fig. 1. The examined fixed-wing aircraft: Cessna-185 Skywagon.

The cross section of its wing airfoil (coded by NACA0012) with the 0° angle of attack (AOA) and the corresponding cylinder can be seen in *Fig. 2*. The difference of curvature between the leading edge segment of airfoil and the cylinder is neglectable, so this approximation can be a good choice in our model.

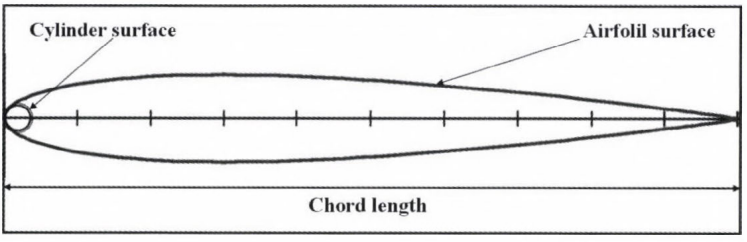

Fig. 2. The cross section of an airfoil and a corresponding cylinder which has the same curvature along the leading edge zone.

The calculation of corresponding cylinder diameter in the case of a given airfoil is based on the method of *Abbott* and *von Doenhoff* (1959):

$$D_c = 2kc, \tag{15}$$

where k is the leading edge radius and the c is the chord length. The data of examined aircraft can be found in *Table 1* (*Lambert*, 1994). As it can be seen, the chord length varies between 1.14 m (wingtip) and 1.63 m (root), so we used 1.385 m as an averaged value, because this number represents the middle segment of wing far enough from the fuselage. Thus, the used leading edge radius of the NACA0012 airfoil was 0.017. Applying Eq. (15) we received the corresponding cylinder diameter value of 0.04709 m. The speed limits of the Cessna-185 aircrafts are 25 m s^{-1} and 80 m s^{-1}, thus, we examined this *TAS* interval in our work (*Table 1*).

Table 1. Some important parameters of the examined fixed-wing aircraft Cessna -185 Skywagon II

Aircraft	Cessna -185 Skywagon II
Wingspan (m)	10.92
Airfoil type	NACA0012
Chord length (m)	1.14 – 1.63
Stall speed (m s^{-1})	25
Maximum speed (m s^{-1})	80
Maximum ceiling (m)	5455

In order to produce real physical (meteorological) background for our examination (as far as possible), we analyzed AIREP icing data between January 1, 2006 and December 31, 2010 over the middle part of Hungary using the atmospheric sounding data of Budapest during this period. There were many icing situations on different air pressure levels, temperatures, and microphysical conditions, and we selected a typical severe icing event of January 14, 2006 which was in connection with thick low level stratiform clouds under a strong inversion layer (cold-pool-like weather situation over the Carpathian Basin) (*Table 2*).

Table 2. AIREP reports during icing situations of January 14, 2006. The icing phenomenon is signed by bold underlined setting

Date and time	**AIREP text**
12:57:26 UTC, January 14, 2006	**SEV ICING** BTN GRD AND 2000FT ON 31R FINAL BY B737
15:28:58 UTC January 14, 2006	**SEV ICING** BTN GRD AND 5000FT ON 13R FINAL BY B737
18:56:52 UTC January 14, 2006	**SEV ICING** BTN 5000FT AND GROUND ON FINAL 13R

As it can be seen, the icing zones were located between the ground and 2000 ft (600 m) and later 5000 ft (1500 m) on January 14, 2006 (*Fig. 3*). We have to note that severe icing for a Boeing-737 does not mean the same icing severity occurrence for other aircrafts!

Based on the mentioned data, our examined air temperature values were –3 °C, –5 °C, and –7 °C, and air pressure values 1010, 970, and 890 hPa, respectively (*Fig. 3*).

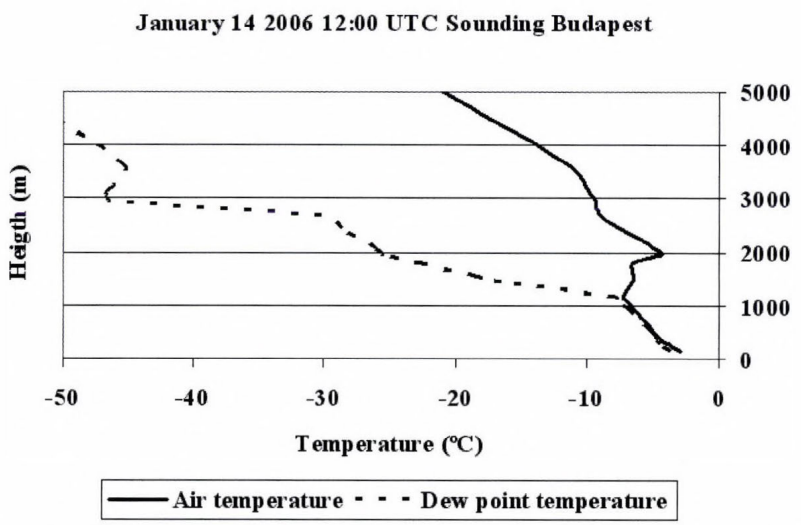

Fig. 3. Vertical air temperature and dew point temperature profiles of January 14, 2006 during AIREP based icing phenomena.

Taking into account the given cloud structure in which the icing was detected by some aircrafts on the mentioned day, we supposed a typical cloud water droplet size distribution (Γ-distribution, *Geresdi*, 2004) with 20 μm median volume diameter (*MVD*), and we also assumed that this distribution was constant in the cloud. On the other hand, the used (presumed) liquid water content (*LWC)* values were 0.2 g kg^{-1} and 0.5 g kg^{-1} in our calculation. The applied values of cloud droplet size distribution and *LWC* in the thick low stratus are in tune with the measurements of *Kunkel* (1971), the work of *Jeck* (2002), and the numerical simulation of *Geresdi* and *Rasmussen* (2005).

We also supposed a 5 minutes hypothetical flight time of our aircraft under selected meteorological condition, because this time interval is not longer than used in the experimentally tested ice accretion model (*Lozowski et al.*, 1983b).

4. Results and discussion

First of all, we calculated the ice accumulation and its rate along the airfoil (cylinder) surface under the given meteorological conditions at 12 UTC on January 14, 2006 over Budapest. Our results – regarding the ice growth intensity values – are in *Table 3*. The *TAS* (tone airspeed of aircraft) as well as the *U*

(freestream velocity) were 60 m s^{-1} and the applied icing severity categories were the international standards by *Jeck* (1998), which are similar to ICAO ones. In spite of the same icing intensity category (moderate), it can be seen that the maximum icing growth intensity values vary between 0.436 and 1.249 mm min^{-1}. The largest value is three times higher than the smallest one, so the moderate marking of icing severity is not always enough to sign this phenomenon exactly. Obviously the higher values can be found at higher *LWC*, because the amounts of impinging droplets are proportional to *LWC* values.

Table 3. The calculated maximum ice growth intensity and severity under different meteorological conditions at 12 UTC on January 14, 2006 over Budapest

Temperature (°C)	Pressure (hPa)	LWC (g kg^{-1})	Ice growth intensity (mm min^{-1})	Icing severity
–3	1010	0.0002	0.51	Moderate
–3	1010	0.0005	1.25	Moderate
–5	970	0.0002	0.44	Moderate
–5	970	0.0005	1.20	Moderate
–7	890	0.0002	0.44	Moderate
–7	890	0.0005	1.17	Moderate

Supposing that the *LWC* was a constant value of 0.0005 g kg^{-1}, the aircraft flew at the 970 hPa pressure level, and the ambient temperature was –5 °C we were able to estimate the icing intensities with different *TAS* values, too.

Our results can be seen in *Table 4*. Under conditions from 30 m s^{-1} to 60 m s^{-1} *TAS* values,the maximum icing rate is moderate, but if the aircraft reaches 70 m s^{-1} *TAS* value the icing rate is severe! We examined the *TAS* values when the icing rate changes from moderate to severe and from light to moderate. In the examined case the moderate/severe limit *TAS* value is 64 m s^{-1}, and the light/moderate one is 28 m s^{-1}. Allowing for Cessna-185 speed limits (*Table 1*), we can establish light (25–27 m s^{-1}), moderate (28–63 m s^{-1}) or severe (64–80 m s^{-1}) icing situations as a function of speed of flight during the same meteorological conditions! The thickness of accreted ice layer varies between 1.75 mm and 8.25 mm after 5 minutes flight time, thus, the amount of ice layer may reach the dangerous thickness (near maximum *TAS*) during a short time period (within 15 minutes).

However, the estimated ice growth intensity is not enough to predict the exact icing risk potential for a given aircraft, because the spatial distribution of the ice layer has a crucial effect in the disturbance of airflow around the wing (*Bragg et al.*, 2005). While the icing process is dry-growth ($n=1$), the geometry of accreted ice layer mainly elliptical with its maximum ice growth at the leading edge, supposing 0° AOA (at the stagnation point or leading edge) (*Lozowski*, 1983a; *Tsao* and *Anderson*, 2005). On the other hand, if the icing process is already wet-growth, the unfrozen part of the collided droplets begin to

move from the leading edge along the airfoil's surface and it may freeze at the farther part of the wing causing the dangerous horn-shaped ice accretion instead of the elliptical one (*Fig. 4*).

Table 4. Icing severity conditions of Cessna-185 aircraft as a function of *TAS* under given constant meteorological conditions (T_a = –5 °C; p = 970 hPa; LWC = 0.0005 g kg^{-1})

TAS (m s^{-1})	Icing growth intensity (mm min^{-1})	Thickness of ice layer after 5 minutes flight (mm)	Icing severity
25	0.35	1.75	Light
30	0.48	2.41	Moderate
40	0.72	3.60	Moderate
50	0.95	4.76	Moderate
60	1.18	5.92	Moderate
70	1.41	7.07	Severe
80	1.65	8.25	Severe

The fundamental problems of an aircraft which has a similar horn-shaped ice contamination on its wing during flight are the extremely high drag force and mainly the loss of lift force because of the appearance of strongly turbulent airflow behind the big ice horns (between the ice horn and the airflow trajectory reattachment zone) (*Fig. 4*). This lift force degradation may reach the 30–40% of the clear (non-contaminated) value (*Cooper et al.*, 1984; *Bragg et al.*, 2005).

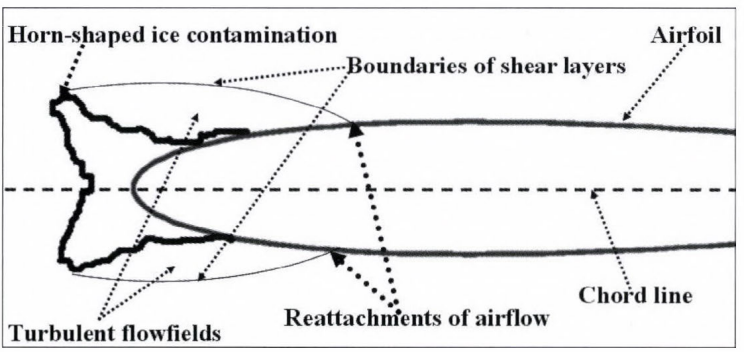

Fig. 4. The geometry of horn-shaped ice contamination and its effect on the airflow around NACA0012 airfoil.

It is clear that the correct estimation of accreted ice layer under different meteorological conditions requires the prediction of geometry of contaminated surface, too. In our work, we described a 2D estimation of the structural icing geometry of a given type of aircraft under measured (T_a, p) and supposed (LWC, U, and droplet size distribution) ambient conditions as it can be seen in *Fig. 5*.

There are some important notes associated with the two calculated cases:

- At higher air temperature (T_a = –3 °C, near 0 °C), the ice envelopes have horn-like shape and this form is more significant at higher speed (*TAS* (*U*) = 50 and 80 m s^{-1}). It is caused by the large amount of runback water (wet-growth icing) moving along the airfoil surface and freezing farther from the stagnation point (leading edge) (*Fig. 5*, right).

- At maximum airspeed (*TAS* (*U*) = 80 m s^{-1}), we can see the horn-shaped ice contamination around the cylinder (airfoil) in both cases, but the distance of the location of maximum accretion from the stagnation point and the maximum of accreted ice thickness are different. When T_a = –7 °C (*Fig. 5*, left), the amount of runback water is smaller, thus, the ice horn is also thinner and its position is closer to the stagnation point (leading edge) than in the other case (T_a = –3 °C).

- When the airspeed is close to the minimum value of Cessna-185 (*TAS* = 25 m s^{-1}), the ice accretion geometry has the elliptical form in both cases, because the icing is dry-growth yet. It is clear that this shape causes less significant anomalies in airflow around the wing than the horn-iced one (*Fig. 5*, right and left).

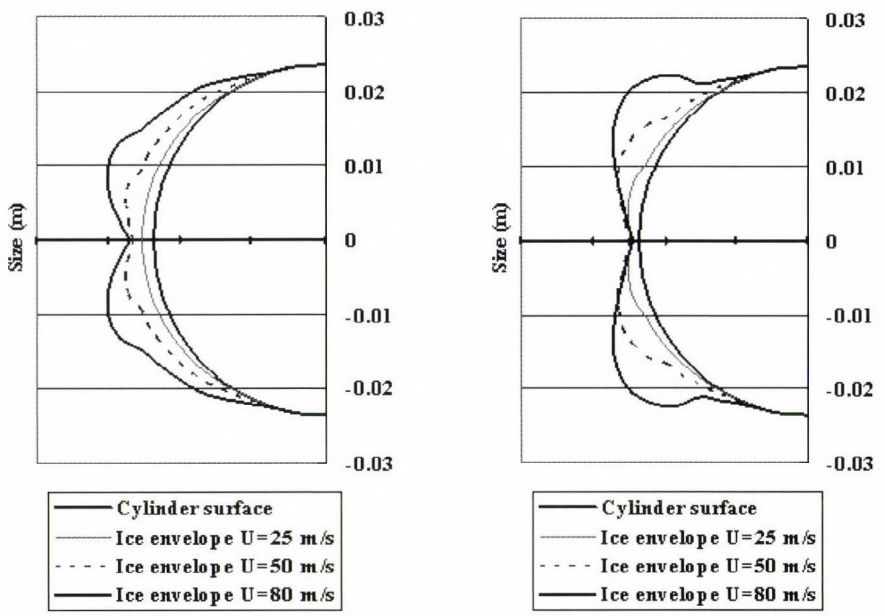

Fig. 5. The 2D geometry of computed accreted ice layers on the surface of the given cylinder (airfoil) after 5 minutes flight time. Left: T_a = –7 °C; p = 890 hPa; LWC = 0.0005 g kg^{-1}; Right: T_a = –3°C; p = 1010 hPa; LWC = 0.0005 g kg^{-1}.

As long as the geometrical effects are initially constants, the environmental parameters may vary along wide ranges during the flight. It follows that the provision of a responsible quasi real-time prediction in the matters of rate, amount, and geometry of airframe ice accretion requires the good knowledge of meteorological (cloud microphysical) conditions and flight plan (airspeed, duration, and 3D route of flight), together. On the other hand, the necessary high resolution values of signed meteorological variables can be produced by a meso-scale numerical weather model such as WRF with a corresponding parameterization or a coupled microphysical model (*Skamarock et al.*, 2005; *Geresdi et al.*, 2001; *Rasmussen* and *Geresdi*, 2005).

Finally, we have to note that further additional studies are necessary to generate the corresponding high resolution meteorological fields of the mentioned ambient physical variables for operational use of our ice accretion model.

5. Summary

On the basis of the described model and our results, we are able to estimate the concrete icing rate and geometry on the wings of a given fixed-wing aircraft during a relatively short time period. There is also a good advantage to calculate the correct limits of the icing severities regarding to given meteorological, aerodynamical and geometrical conditions (aircraft-dependent estimations).

Applying the calculated geometry (shape) of the accreted ice layer, we are able to predict the most dangerous horn-iced phenomena and its probable location within the cloud.

The effectively accreted ice characteristics highly depend on flight time as well. Knowing the flight environment, we may derive a maximum flight time for a given fixed-wing aircraft during this situation without any dangerous icing (flight path optimization).

Moreover, the embedding of a similar ice accretion model (such as described one) into an operative forecasting procedure can level up the usage and reliability of icing predictions and may lead to higher level of flight safety.

Acknowledgements—The author thanks *István Geresdi* and *Ferenc Wantuch* for useful suggestions and comments on work, *Péter Szalóky* and *Péter Kardos* for providing AIRMET data set.

References

Abbott, I. H. and *von Doenhoff, A.E.*, 1959: *Theor. Wing Sections*. Dover, New York.

Achenbach, E., 1977: The effect of surface roughness on the heat transfer from circular cylinders to the cross flow of air. *Int. J. Heat Mass Transfer 20,* 359-369.

Bragg, M.B., Broeren, A.P. and *Blumenthal, L.A.*, 2005: Iced-airfoil aerodynamics. *Prog. Aerospace Sci. 41*, 323-362.

Cooper, W.A., Sand, W.R., Politovich, M.K. and *Veal, D.L.*, 1984: Effects of Icing on Performance of a Research Aircraft. *J. Aircraft 21*, 708-715.

Finstad, J.K., Lozowski, E.P. and *Gates, E.M.*, 1988: A computational investigation of water droplet trajectories. *J. Atmos. Ocean. Tech. 5*, 160-170.

Fuchs, W., 2003: Forecast of aircraft icing by use of boundary layer model products: First experiences. *Proceedings of The 13th International Offshore and Polar Engineering Conference*. Honolulu, USA, 423-428.

Fuchs, W. and *Lütkebohmert, M.*, 2001: Aircraft icing forecast. *Proceedings of The 11th International Offshore and Polar Engineering Conference*. Stavanger, Norway, 686-689.

Gent, R.W., Markiewicz, R.H. and *Cansdale, J.T.*, 1987: Further studies of helicopter rotor ice accretion and protection. *Vertica 11*, 473-492.

Gent, R.W., Dart, N.P. and *Cansdale, J.T.*, 2000: Aircraft icing. *Phil. Trans. Roy. Soc. London. A. 358*, 2873-2911.

Geresdi, I., 2004: *Cloudphysics* (in Hungarian). Dialóg Campus Kiadó. Budapest – Pécs.

Geresdi, I. and *Rasmussen, R.M.*, 2005: Freezing drizzle formation in stably Stratified layer clouds: The role of giant nuclei and aerosol particle size distribution and solubility. *J. Atmos. Sci. 62*, 2037-2067.

Geresdi, I. Rasmussen, R.M., Thompson, G., Manning, K., and *Karplus, E.*, 2001: Freezing drizzle formation in stably stratified layer clouds: The role of radiative cooling of cloud droplets, cloud condensation nuclei, and ice initiation. *J. Atmos. Sci. 59*, 837-860.

Jeck, R., 1998: A workable, aircraft-specific icing severity scheme. Appendix A. *Preprints of AIAA-98-0094. 36th Aerospace Sciences Meeting and Exhibit*. Reno, USA, 1-12.

Jeck, R., 2002: Icing Design Envelopes (14 CFR Parts 25 and 29, Appendix C) Converted to a Distance-Based Format. *Final Report of U.S. Department of Transportation Federal Aviation Administration Office of Aviation Research*. Washington, USA, 1-48.

Kunkel, B.A., 1971: Fog drop-size distributions measured with a laser hologram camera. *J. Appl. Meteorol. 10*, 482-486.

Lambert, M. (ed.), 1994: *Jane's All theWorld's Aircrafts*. Jane's Publishing Co., London, UK.

Langmuir, I. and *Blodgett, K.B.*,1946: A mathematical investigation of water droplet trajectories. *Collected Works of Irving Langmuir*. 10. Pergamon Press, 348-393.

Lankford, T.T., 2001: *Aviation Weather Handbook*. McGraw-Hill, New York.

Launiainen, J. and *Lyyra, M.*, 1986: Icing on a non-rotating cylinder under conditions of high liquid water content in the air: II. Heat transfer and rate of ice growth. *J. Glaciol. 32*, 12-19.

List, R., 1977: Ice acretions on structures. *J. Glaciol. 19*, 451-465.

Lozowski, E.P., Stallabrass, J.R., and *Hearty, P.F.*, 1983a: The icing of an unheated nonrotating cylinder. Part I: A simulation model. *J. Clim. Appl. Meteorol. 22*, 2053-2062.

Lozowski, E.P., Stallabrass, J.R., and *Hearty, P.F.*, 1983b: The icing of an unheated nonrotating cylinder. Part II: Icing wind tunnel experiments. *J. Clim. Appl. Meteorol. 22*, 2063-2074.

Ludlam, F.H., 1951: The heat economy of a rimed cylinder. *Q. J. Roy. Meteor. Soc. 77*, 663-666.

Makkonen, L., 1981: Estimating intensity of atmospheric ice accretion on stationary structures. *J. Appl. Meteorol. 20*, 595-600.

Makkonen, L. and *Stallabrass, J.R.*, 1987: Experiments on the cloud droplet collision efficiency of cylinders. *J. Clim. Appl. Meteorol. 26*, 1406-1411.

Mazin, I.P., Korolev, A.V., Heymsfield, A., Isaac, G.A. and *Cober, S.G.*, 2001: Thermodynamics of icing cylinder for measurements of liquid water content in supercooled clouds. *J. Atmos. Ocean. Tech. 18*, 543-558.

Messinger, B.L., 1953: Equilibrium temperature of an unheated icing surface as a function of airspeed. *J. Aeronaut. Sci. 20*, 29-41.

Rasmussen, R.M., and *Geresdi, I.* 2005: Freezing drizzle formation in stably stratified layer clouds. Part II: The role of giant nuclei and aerosol particle size distribution and solubility. *J. Atmos. Sci. 62*, 2037-2057.

Saeed, F., 2000: State-of-the-art aircraft icing and anti-icing simulation. *ARA J. 25-27*, 106-113.

Seban, R.A., 1960: The influence of free stream turbulence on the local heat transfer from cylinders. *J. Heat Trans. 82*, 101-107.

Skamarock, W.C., Klemp, J.B., Dudhia, J., Gill, D.O., Barker, D.M., Wang, W. and *Powers, J.G.*, 2005: A *Description of the Advanced Research WRF Version 2*. NCAR Technical. Note, Boulder, USA, 1-88.

Tsao J-C., and *Anderson, D.N.*, 2005: Additional study of water droplet median volume diameter (MVD) effects on ice shape. *NASA/CR-2005-213853 report*, 1-11.

IDŐJÁRÁS

VOLUME 115 * 2011

EDITORIAL BOARD

AMBRÓZY, P. (Budapest, Hungary)
ANTAL, E. (Budapest, Hungary)
BARTHOLY, J. (Budapest, Hungary)
BATCHVAROVA, E. (Sofia, Bulgaria)
BRIMBLECOMBE, P. (Norwich, U.K.)
CZELNAI, R. (Dörgicse, Hungary)
DUNKEL, Z. (Budapest, Hungary)
FISHER, B. (Reading, U.K.)
GELEYN, J.-Fr. (Toulouse, France)
GERESDI, I. (Pécs, Hungary)
GÖTZ, G. (Budapest, Hungary)
HASZPRA, L. (Budapest, Hungary)
HORÁNYI, A. (Budapest, Hungary)
HORVÁTH, Á. (Siófok, Hungary)
HORVÁTH, L. (Budapest, Hungary)
HUNKÁR, M. (Keszthely, Hungary)
LASZLO, I. (Camp Springs, MD, U.S.A.)
MAJOR, G. (Budapest, Hungary)
MATYASOVSZKY, I. (Budapest, Hungary)
MÉSZÁROS, E. (Veszprém, Hungary)
MIKA, J. (Budapest, Hungary)
MERSICH, I. (Budapest, Hungary)
MÖLLER, D. (Berlin, Germany)
NEUWIRTH, F. (Vienna, Austria)
PINTO, J. (Res. Triangle Park, NC, U.S.A.)
PRÁGER, T. (Budapest, Hungary)
PROBÁLD, F. (Budapest, Hungary)
RADNÓTI, G. (Budapest, Hungary)
S. BURÁNSZKI, M. (Budapest, Hungary)
SIVERTSEN, T.H. (Risør, Norway)
SZALAI, S. (Budapest, Hungary)
SZEIDL, L. (Budapest, Hungary)
SZUNYOGH, I. (College Station, TX, U.S.A.)
TAR, K. (Debrecen, Hungary)
TÄNCZER, T. (Budapest, Hungary)
TOTH, Z. (Camp Springs, MD, U.S.A.)
VALI, G. (Laramie, WY, U.S.A.)
VARGA-HASZONITS, Z. (Mosonmagyaróvár, Hungary)
WEIDINGER, T. (Budapest, Hungary)

Editor-in-Chief
LÁSZLÓ BOZÓ

Executive Editor
MARGIT ANTAL, MÁRTA T. PUSKÁS

BUDAPEST, HUNGARY

AUTHOR INDEX

TABLE OF CONTENTS

I. Papers

II. Book review

III. News

SUBJECT INDEX

INSTRUCTIONS TO AUTHORS OF *IDŐJÁRÁS*

The purpose of the journal is to publish papers in any field of meteorology and atmosphere related scientific areas. These may be

- research papers on new results of scientific investigations,
- critical review articles summarizing the current state of art of a certain topic,
- short contributions dealing with a particular question.

Some issues contain "News" and "Book review", therefore, such contributions are also welcome. The papers must be in American English and should be checked by a native speaker if necessary.

Authors are requested to send their manuscripts to

Editor-in Chief of IDŐJÁRÁS
P.O. Box 38, H-1525 Budapest, Hungary
E-mail: journal.idojaras@met.hu

including all illustrations. MS Word format is preferred in electronic submission. Papers will then be reviewed normally by two independent referees, who remain unidentified for the author(s). The Editor-in-Chief will inform the author(s) whether or not the paper is acceptable for publication, and what modifications, if any, are necessary.

Please, follow the order given below when typing manuscripts.

Title page: should consist of the title, the name(s) of the author(s), their affiliation(s) including full postal and e-mail address(es). In case of more than one author, the corresponding author must be identified.

Abstract: should contain the purpose, the applied data and methods as well as the basic conclusion(s) of the paper.

Key-words: must be included (from 5 to 10) to help to classify the topic.

Text: has to be typed in single spacing on an A4 size paper using 14 pt Times New Roman font if possible. Use of S.I. units are expected, and the use of negative exponent is preferred to fractional sign. Mathematical formulae are expected to be as simple as possible and numbered in parentheses at the right margin.

All publications cited in the text should be presented in the *list of references*, arranged in alphabetical order. For an article: name(s) of author(s) in Italics, year, title of article, name of journal, volume, number (the latter two in Italics) and pages. E.g., *Nathan, K.K.,* 1986: A note on the relationship between photosynthetically active radiation and cloud amount. *Időjárás 90,* 10-13. For a book: name(s) of author(s), year, title of the book (all in Italics except the year), publisher and place of publication. E.g., *Junge, C.E.,* 1963: *Air Chemistry and Radioactivity.* Academic Press, New York and London. Reference in the text should contain the name(s) of the author(s) in Italics and year of publication. E.g., in the case of one author: *Miller* (1989); in the case of two authors: *Gamov* and *Cleveland* (1973); and if there are more than two authors: *Smith et al.* (1990). If the name of the author cannot be fitted into the text: *(Miller,* 1989); etc. When referring papers published in the same year by the same author, letters a, b, c, etc. should follow the year of publication.

Tables should be marked by Arabic numbers and printed in separate sheets with their numbers and legends given below them. Avoid too lengthy or complicated tables, or tables duplicating results given in other form in the manuscript (e.g., graphs).

Figures should also be marked with Arabic numbers and printed in black and white or color (under special arrangement) in separate sheets with their numbers and captions given below them. JPG, TIF, GIF, BMP or PNG formats should be used for electronic artwork submission.

Reprints: authors receive 30 reprints free of charge. Additional reprints may be ordered at the authors' expense when sending back the proofs to the Editorial Office.

More information for authors is available: journal.idojaras@met.hu

Published by the Hungarian Meteorological Service

Budapest, Hungary

INDEX 26 361

HU ISSN 0324-6329